RESEARCH ARTICLE

Key Points:
- The relationship between global satellite land surface temperature (LST) and ground-based air temperature (T_{2m}) over land is characterized
- Geographical location, land cover type, vegetation fraction, and elevation strongly influence the LST-T_{2m} relationship
- Correlation between the global time series of LST and T_{2m} anomalies is 0.9 and 90% of the LST anomalies fall within the T_{2m} uncertainties

Correspondence to:
E. J. Good,
elizabeth.good@metoffice.gov.uk

A spatiotemporal analysis of the relationship between near-surface air temperature and satellite land surface temperatures using 17 years of data from the ATSR series

Elizabeth J. Good[1] iD, **Darren J. Ghent[2]** iD, **Claire E. Bulgin[3]** iD, and **John J. Remedios[2]** iD

[1]Met Office Hadley Centre, Exeter, UK, [2]National Centre for Earth Observation, Department of Physics and Astronomy, University of Leicester, Leicester, UK, [3]Department of Meteorology, University of Reading, Reading, UK

Abstract The relationship between satellite land surface temperature (LST) and ground-based observations of 2 m air temperature (T_{2m}) is characterized in space and time using >17 years of data. The analysis uses a new monthly LST climate data record (CDR) based on the Along-Track Scanning Radiometer series, which has been produced within the European Space Agency GlobTemperature project (http://www. globtemperature.info/). Global LST-T_{2m} differences are analyzed with respect to location, land cover, vegetation fraction, and elevation, all of which are found to be important influencing factors. LST_{night} (~10 P.M. local solar time, clear-sky only) is found to be closely coupled with minimum T_{2m} (T_{min}, all-sky) and the two temperatures generally consistent to within ±5°C (global median LST_{night}-T_{min} = 1.8°C, interquartile range = 3.8°C). The LST_{day} (~10 A.M. local solar time, clear-sky only)-maximum T_{2m} (T_{max}, all-sky) variability is higher (global median LST_{day}-T_{max} = −0.1°C, interquartile range = 8.1°C) because LST is strongly influenced by insolation and surface regime. Correlations for both temperature pairs are typically >0.9 outside of the tropics. The monthly global and regional anomaly time series of LST and T_{2m}—which are completely independent data sets—compare remarkably well. The correlation between the data sets is 0.9 for the globe with 90% of the CDR anomalies falling within the T_{2m} 95% confidence limits. The results presented in this study present a justification for increasing use of satellite LST data in climate and weather science, both as an independent variable, and to augment T_{2m} data acquired at meteorological stations.

Plain Language Summary Surface temperatures over land have traditionally been measured at weather stations. There are many parts of the globe where there are very few stations, for example across much of Africa and Antarctica, leading to gaps in surface temperature datasets, affecting our understanding of how surface temperatures are changing, and the impacts of extreme events (e.g. heat waves). Satellites can provide temperature observations across the globe. However, satellites measure how hot the land surface temperature (LST; including the uppermost parts of e.g. trees, buildings) are to touch, whereas weather stations measure the air temperature just above the surface (T2m). Additionally, satellite LST data may only be available in cloud-free conditions. This paper describes a comparison between T2m and a new 17-year LST dataset. It demonstrates that LST and T2m are often strongly related, particularly at night, but the exact relationship depends on location, land surface type, vegetation and elevation. A time-series analysis shows that the change in LST and T2m with time is remarkably similar; giving confidence in the T2m trends reported elsewhere in the climate change literature, as these datasets are independent. The results of this study demonstrate that LST can usefully augment T2m observations in climate and weather science.

1. Introduction

Land surface temperature (LST)—the temperature of the land surface rather than that of the near-surface air—is a key surface parameter in driving boundary layer processes and has recently been proposed in the 2016 Global Climate Observing System Implementation Plan as a new essential climate variable [*GCOS*, 2016]. LST observations are most readily available from spaceborne radiometers that operate at infrared (IR) or microwave (MW) wavelengths offering complete global coverage at spatial scales ranging from a few tens of meters (IR) to a few tens of kilometers (MW), with a temporal frequency of around twice per month to once every 15 min.

Applications for satellite-derived LST are now widely reported in the literature. Examples include using LST to evaluate land surface models [*Koch et al.*, 2016], improve the performance of numerical weather prediction

models [*Singh et al.*, 2016], diagnose surface response to dry spells [*Folwell et al.*, 2016], assess drought [*Karnieli et al.*, 2010; *Mühlbauer et al.*, 2016], characterize urban heat islands [*Azevedo et al.*, 2016; *De Ridder et al.*, 2012; *Dousset et al.*, 2011; *Hu and Brunsell*, 2013], and to estimate near-surface air temperature in the absence of meteorological stations [*Chen et al.*, 2014; *Good*, 2015; *Kilibarda et al.*, 2014]. Operational LST data sets are now available from several sensors, some of which extend for more than a decade in length. This includes LST data sets from the widely used Moderate Resolution Imaging Spectroradiometer (MODIS) onboard the polar-orbiting Terra (2000–present) and Aqua (2002–present) platforms [*Wan*, 2013, 2014] and the Spinning Enhanced Visible and Infrared Imager (SEVIRI) onboard the geostationary Meteosat Second Generation platforms (2005–present) [*Trigo et al.*, 2008; *Freitas et al.*, 2010, *Freitas et al.*, 2013].

Use of satellite LST within the climate community, however, has not yet become widespread, and there are very few examples in the literature where LST has been used to investigate climatic temperature change [*Jiménez-Muñoz et al.*, 2013; *Jin*, 2004; *Oku et al.*, 2006]. One of the main obstacles to this has been the absence of long-term, high-quality, stable LST climate data records (CDRs). Another barrier has been a lack of understanding of what satellite LSTs represent and how this relates to the near-surface air temperature measured at weather stations (T_{2m}), which has traditionally been the variable of choice over land in assessing surface temperature response to climate change [*Caesar et al.*, 2006; *Hansen et al.*, 2010; *Jones et al.*, 2012; *Smith et al.*, 2008] and evaluating climate models [*Box and Rinke*, 2003; *Kiktev et al.*, 2003; *Kharin et al.*, 2005]. However, in contrast, the use of satellite observations of sea surface temperature (SST)—which are similar in principle to satellite LST observations—in climate science is well established [e.g., *Good et al.*, 2007; *Høyer and Karagali*, 2016; *Rayner et al.*, 2003]; *Reynolds et al.*, 2002] and SST CDRs already exist for some sensors [*Casey et al.*, 2010; *Merchant et al.*, 2012; *Merchant et al.*, 2014].

Following the success of satellite SST CDRs, increasing user interest in satellite LST data sets, lengthening satellite records, and improvements to LST retrieval techniques, LST data providers have naturally started to look toward generating CDRs. One such initiative includes creating the first multidecadal LST CDR from the Meteosat first- and second-generation geostationary satellite series, which has provided reliable thermal IR observations over Europe, Africa, and parts of South America since the early 1980s [*Duguay-Tetzlaff et al.*, 2015]. There has also been movement toward creating a long-term MW LST record, which could provide LSTs back to 1987 using data from the Special Sensor Microwave/Imagers [*Prigent et al.*, 2016]. MW LSTs have the benefit of providing LST observations in all nonprecipitating conditions, whereas IR LSTs are limited to cloud-free scenes. However, the accuracy and spatial resolution of IR LSTs are superior to MW LSTs, making them more suitable for many applications.

The most accurate satellite LST data sets are derived from sensors that have two or more thermal IR channels; these channels typically include the "split-window" channels, which are located at approximately 11 and 12 μm. This enables an improved atmospheric correction to be made compared with single-channel IR retrievals, as atmospheric attenuation varies with wavelength [*Dash et al.*, 2002; *Li et al.*, 2013]. One such sensor that provided this capability is the Along-Track Scanning Radiometer (ATSR), which had unprecedented radiometric accuracy and stability (section 2.1) and a record length that exceeds 20 years. Together with a very stable orbit with little temporal drift (per sensor), these factors make the ATSR series a desirable target for generation of an LST CDR. The first ATSR LST CDR has been produced within the framework of the European Space Agency's (ESA) GlobTemperature project (http://www.globtemperature.info/), and it is version 1.0 of this data set that is analyzed in this study.

The analyses presented here comprise two aspects. First, the worldwide LST-T_{2m} differences are characterized by comparing the ATSR CDR with in situ T_{2m} observations, in both point-station and in gridded form. Several studies now exist in the literature where the LST-T_{2m} relationship is explored through the analysis of satellite LST observations and coincident ground-based observations of T_{2m} [e.g., *Hachem et al.*, 2012; *Mildrexler et al.*, 2011; *Sohrabinia et al.*, 2014; *Urban et al.*, 2013; *Vancutsem et al.*, 2010]. A few studies also examine this relationship using ground-based observations of both LST and T_{2m} [e.g., *Gallo et al.*, 2011; *Good*, 2016]. However, these studies have tended to be focused, for example, on specific geographical regions [*Hachem et al.*, 2012; *Sohrabinia et al.*, 2014; *Urban et al.*, 2013; *Vancutsem et al.*, 2010] or stations [*Gallo et al.*, 2011; *Good*, 2016,], or a particular aspect of the LST-T_{2m} relationship. For example, *Mildrexler et al.* [2011] present an analysis of the global relationship between the annual maximum LST and T_{2m} using 7 years of data from MODIS/Aqua, which has a local solar overpass time of ~1:30 P.M. More recently, *Lian et al.*

[2017] used 12 years of MODIS/Aqua data to analyze the global relationship between maximum monthly T_{2m} (T_{max}) and monthly maximum LST.

This study complements previous studies by providing new information on the relationship between data sets for LST and T_{2m}—including the relationship between nighttime LST (LST_{night}) and T_{min}—on a global scale as a function of land cover type, vegetation fraction, and elevation. This study is based on ~17 years of data from the ATSR, which has not yet been used to study the LST-T_{2m} relationship in detail.

The second part of this paper looks at the temporal evolution of the global mean LST compared to the equivalent T_{2m} time series, which has not been addressed in the existing literature. Previous studies analyzing LST time series are scarce and tend to be limited to specific geographical regions and focus only on LST. For example, *Jiménez-Muñoz et al.* [2013] analyze 13 years of LST data from MODIS and ERA-Interim skin temperatures over the Amazon, while *Oku et al.* [2006] analyze 7 years of LST acquisitions from the Geostationary Meteorological Satellite 5 over the Tibetan Plateau.

LST is a challenging parameter to estimate from satellite observations, owing to the variation and uncertainty in surface emissivity and atmospheric attenuation, which must be known precisely to retrieve LST accurately [*Dash et al.*, 2002; *Li et al.*, 2013]. The accuracy of current operational IR-based data sets is typically 1–3°C [*Duguay-Tetzlaff et al.*, 2015; *Freitas et al.*, 2013; *Trigo et al.*, 2008; *Wan*, 2014], which is considerably lower than for IR SST retrievals that can achieve accuracies of close to 0.1°C [*Embury et al.*, 2012]. The spatial heterogeneity of LST and land T_{2m} is high, particularly during the day owing to differential solar heating, vegetation transpiration, and surface turbulence. As a result, variations of several °C between neighboring stations and across single-satellite pixels are observed [*Good*, 2015; *Yan et al.*, 2010]. These are important factors to consider when comparing satellite LSTs with station-based T_{2m} estimates, as they will lead to inherent differences of up to a few °C.

Previous studies show that LST and T_{2m} are generally well coupled, with correlation coefficients that usually exceed 0.6 and very often 0.8. LST and T_{2m} are most tightly coupled over highly vegetated surfaces and when insolation is low, for example, under full cloud cover, at night or at high latitudes during winter, spring, and autumn months. In these cases, LST and T_{2m} may differ by only 1–2°C. In contrast, LST can exceed T_{2m} by several °C when insolation is high and vegetation cover is low to moderate [*Good*, 2016; *Hachem et al.*, 2012; *Mildrexler et al.*, 2011; *Sohrabinia et al.*, 2014; *Urban et al.*, 2013; *Vancutsem et al.*, 2010]. In extreme conditions, for example, under clear skies during the middle part of the day at low latitudes over nonvegetated surfaces, the LST-T_{2m} temperature difference may approach or even exceed 20°C [*Good*, 2016; *Mildrexler et al.*, 2011]. Even in these cases, LST and T_{2m} remain coupled albeit with much greater changes in LST for a given change in T_{2m}. It is this coupled relationship that has led to the recent abundance of studies that attempt to use satellite LSTs to help infill gaps in current T_{2m} data sets [*Benali et al.*, 2012; *Chen et al.*, 2014; *Good*, 2015; *Kilibarda et al.*, 2014; *Janatian et al.*, 2016; *Oyler et al.*, 2015; *Parmentier et al.*, 2015; *Zhang et al.*, 2011].

The focus of this study is on the spatial and temporal relationship between LST and T_{2m} on a global scale. The analysis of a >17 year satellite LST record presented here will demonstrate the potential for using LST in climate science, particularly in augmenting information from traditional meteorological T_{2m} observations. (Data from the first 4 years of the ATSR record are not analyzed here owing to ongoing calibration issues.) Section 2 introduces the data sets used in the study, while section 3 summarizes the methods used in analyzing the data. The results of the study are presented in sections 4 to 6, and their implications discussed in section 7. The main conclusions of the study are summarized in section 8.

2. Data

A summary of the data sets used in this study is provided in Table 1. Further details are presented in the following subsections.

2.1. GlobTemperature CDR

The GlobTemperature CDR comprises observations from the Along-Track Scanning Radiometer (ATSR) series [*Llewellyn-Jones et al.*, 2001; *Smith et al.*, 2012]. The ATSR was designed to make accurate observations of sea surface temperature (SST) with channels located within the visible to infrared part of the electromagnetic spectrum, including the split-window channels at approximately 11 and 12 μm for surface temperature

Table 1. Data Sets Used in This Study

Data Set (Version Number)	Coverage	Data Type	Spatial Resolution	Temporal Resolution	Record Start	Record Stop	Variables	Citation
ATSR CDR (v1)	Global land and ice (clear-sky only)	Satellite	0.05°	Monthly	August 1995[a]	March 2012[a]	LST DayLST Night	*Ghent* [2012]
CRUTEM4 (v4.4.0.0)	Global (incomplete)	Station	5.0°	Monthly	Jan 1856	ongoing	T_{mean} anomaly	*Jones et al.* [2012]
CRU TS (v3.23)	Global land (except Antarctica)	Station	0.5°	Monthly	Jan 1901	Dec 2014	T_{mean} T_{max} T_{min}	*Harris et al.* [2014]
GHCN-M (v 3.3.0.20160130.qca)	Global (station time series)	Station	Point	Monthly	Jan 1730	ongoing	T_{mean} T_{max} T_{min}	*Lawrimore et al.* [2011]
MODIS (MOD11C3, v6)	Global land and ice (clear-sky only)	Satellite	0.05°	Monthly	Feb 2000	ongoing	LST DayLST night	*Wan* [2013, 2014]
ERA-Interim	Global (all surfaces)	Reanalysis	~80 km	6-hourly	Jan 1979	Ongoing	Instantaneous skin temperature	*Dee et al.* [2011]
Copernicus/Geoland-2 Fractional Vegetation Cover (v1.0)	Global (clear-sky land only)	Satellite	1/112°	10-day composite	Jan 1999	Dec 2012	Fractional vegetation cover	*Baret et al.* [2013]; *Camacho et al.* [2013]
LC CCI (v1.6)	Global land and ice.	Satellite	300 m	N/A	Jan 1998	Dec 2012	Landcover type	*Bontemps et al.* [2012]; *Poulter et al.* [2015]
SRTM (v1)	Global	Satellite	30 m	N/A	2000	2000	Elevation	*Farr and Kobrick* [2000]; *Rodriguez et al.* [2005]

[a]January–June 1996 and January–June 2001 are not included in the analysis as these are incomplete months in the CDR (see text).

retrieval. The instrument design benefits from an exceptionally stable onboard calibration system with two onboard blackbody targets, and Stirling-cycle cooled detectors, enabling radiometric accuracy of its infrared channels of better than 0.05°C [*Smith et al.*, 2012]. The ATSR was equipped with dual-viewing capability allowing nominally the same point on the Earth's surface to be viewed through two different atmospheric path lengths albeit with slightly differing spatial footprints. For SST retrieval, this is used to improve the correction for atmospheric effects [*Zavody et al.*, 1995]. The ATSR had a swath width of approximately 500 km, achieving all-sky global coverage in 3 days.

ATSR-1 was launched onboard the European Space Agency's first Earth Remote Sensing (ERS-1) satellite in July 1991, with ATSR-2 following onboard ERS-2 in April 1995. The third ATSR, the Advanced ATSR (AATSR), was launched in March 2002 onboard ESA's Envisat satellite, which unfortunately ceased communications on 8 April 2012, bringing an end to the ATSR mission. The AATSR is succeeded by the Sea and Land Surface Temperature Radiometer (SLSTR), which was launched onboard ESA's Sentinel-3 satellite in February 2016. The overpass time of the ATSR series was approximately 10:00 A.M./P.M. (AATSR) to 10:30 A.M./P.M. (ATSR-1; ATSR-2) local solar time. SLSTR also has a local overpass time of 10:00 A.M./P.M.

An operational LST retrieval scheme was first introduced for the AATSR and is described by *Prata* [2002, and references therein]. The operational algorithm is a nadir-only split-window retrieval. The forward view (at ~55° from nadir) is not usually used for LST owing to difficulties in accounting for emissivity dependency on view angle, and LST anisotropy (the observed LST for some surfaces depends on zenith and azimuth observation angles), as well as the collocation issues arising from the spatial mismatch between the forward and nadir footprints noted earlier . A modified version of this algorithm, described in *Ghent* [2012], with improved retrieval coefficients and auxiliary data sets, enhanced cloud masking, and full uncertainty budget, has been implemented within ESA's GlobTemperature project to create a long-term LST data set based on the latter two ATSR instruments (http://www.globtemperature.info/). The CDR is a homogenized version of this data set, providing monthly average global fields of clear-sky LST_{day} and LST_{night} in which a consistent algorithm and cloud detection method is applied to observations from both sensors. Version 1 of the CDR includes only ATSR-2 and AATSR, owing to ongoing calibration issues with parts of the ATSR-1 record.
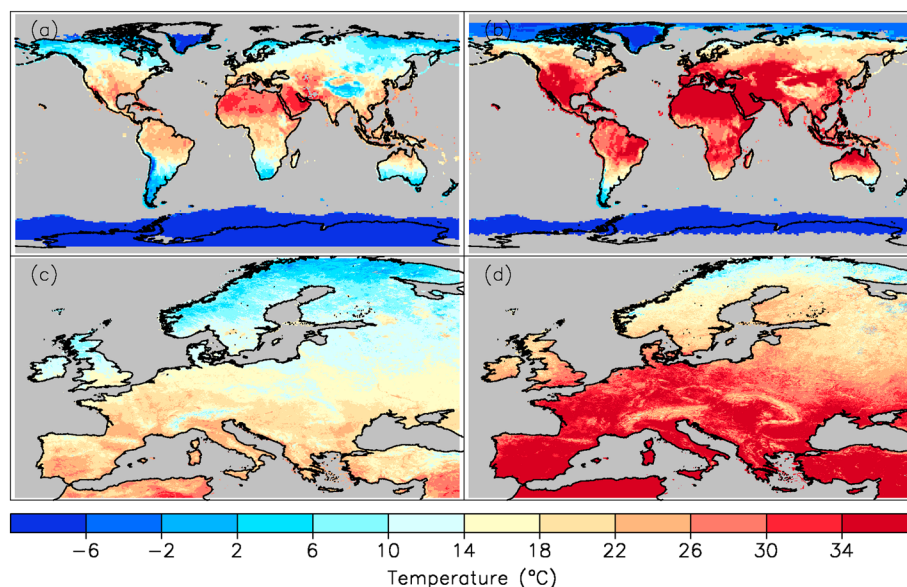
Figure 1. An example of the ATSR CDR for August 2003. (a and c) LST night and (b and d) LST day. Some striping is evident in the data where different orbits have contributed to the monthly average. In Figure 1c the striping is in a top left to bottom right direction corresponding to the ascending node of the ATSR overpass. In Figure 1d the direction is top right to bottom left, corresponding to the descending node.

Uncertainty information is provided within the CDR at 0.05° resolution, accounting for instrument noise, systematic retrieval uncertainties, and surface related components. Surface parameters in the LST retrieval are constrained using the Cooperative Institute for Meteorological Satellite Studies emissivity data set [*Hulley et al.*, 2015], with coefficient fitting to an extended GlobCover land cover classification [*Arino et al.*, 2007]. The uncertainty in the coefficient fitting due to emissivity is 0.01°C, with an additional surface uncertainty component related to fractional vegetation auxiliary data. Emissivity and land cover classification monthly composites are compiled from high-resolution satellite data at 100–300 m resolution, providing global coverage, maximizing the information on surface spatial variability whilst minimizing data gaps due to persistent cloud.

Owing to the 30 min difference in overpass time between ATSR-2 and AATSR, ATSR-2 LSTs in the CDR are adjusted to account for this difference, as LST can change substantially in 30 min, particularly when insolation is high. For LST_{day}, this is essentially a cooling correction for ATSR-2, while for LST_{night}, the correction will usually have a small warming effect. The corrections are derived empirically from the LST differences during ATSR-2/AATSR overlap period (June 2002 to May 2003 inclusive) on a monthly basis for both LST_{day} and LST_{night} on the output 0.05° grid. For 0.05° cells where this LST difference cannot be estimated directly (e.g., due to cloud), and there is a gap in the output grid, the correction is derived from cells with the same land cover within a 10° × 10° tile. The errors associated with implementing this correction are likely to be larger for day time (~0.5°C) compared with nighttime (~0.2°C) owing to the strong dependency of LST on insolation. AATSR is used in preference to ATSR-2 in this study where records from both sensors are present due to the lower radiometric noise levels associated with AATSR brightness temperature compared with those of ATSR-2 [*Smith et al.*, 2012].

An example month of the GlobTemperature ATSR CDR (August 2003) is shown in Figure 1. It is notable in this example that there are no daytime LSTs over Antarctica and no nighttime LSTs at northern high latitudes. This is because daytime and nighttime observations are distinguished in the CDR by solar zenith angle (SZA) and not overpass time, whereas in other satellite LST data sets daytime and nighttime at polar latitudes are distinguished by time of day alone (and not sunlight). This results in no daytime LST field for Antarctica for months where it is dark at 10 A.M., for example. Incompletely observed months within the ATSR record are excluded from the CDR, which includes June and July 1995 (end of commissioning period), January–June 1996 (scan mirror failure), January–June 2001 (gyro failure), and April 2012 (8 April: end of mission).
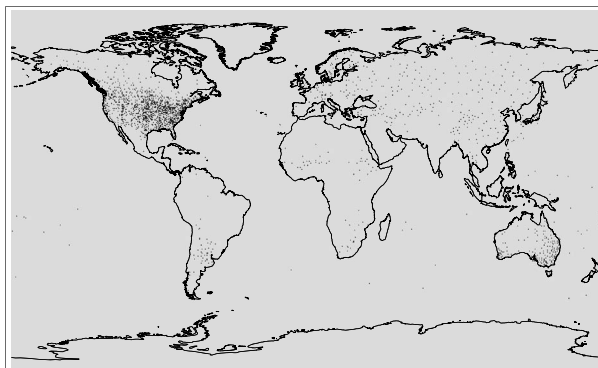
Figure 2. Map of CRU TS stations for the 1995–2012 period.

2.2. Climatic Research Unit Time Series Monthly Gridded T_{2m}

The Climatic Research Unit Time Series (CRU TS; v3.23) is a gridded station data set [*Harris et al.*, 2014]. It consists of monthly time series of a number of variables, including monthly mean (T_{mean}), minimum (T_{min}), and maximum (T_{max}) temperatures at a spatial resolution of 0.5° latitude/longitude. While CRU TS includes many homogenized station records from National Meteorological Services, it is not "specifically homogeneous" and should therefore be treated with caution in time series analysis [*Harris et al.*, 2014]. For this reason, CRU TS is only used for quantifying the spatial and seasonal relationships between LST and T_{2m} in this study. Unlike the CDR, the CRU TS data are "all sky" and include T_{2m} observations under both cloud and clear sky.

2.3. GHCN-Monthly Station T_{2m}

CRU TS is the primary data set used in this study to characterize the spatial and seasonal LST-T_{2m} relationship. However, this is an interpolated data set with larger uncertainties where station density is low (Figure 2). To verify the analysis, station observations from the Global Historical Climate Network Monthly (GHCN-M) v3.3.0.20160130.qca data set are also used. GHCN-M is a collection of 7280 monthly station records produced by the National Centers for Environmental Information (NCEI) in the United States. Version 3 of the "QCA" (quality controlled adjusted) data set is used in this study, which has undergone quality control and includes homogeneity adjustments to correct for nonclimatic changes in the station time series [*Lawrimore et al.*, 2011]. No additional screening of the data is carried out in this study since any data that have failed quality checks or have too many inhomogeneities in the record are replaced by missing-data indicators in the GHCN-M data records. GHCN-M includes monthly all-sky T_{mean}, T_{min}, and T_{max} and has been used by the Intergovernmental Panel on Climate Change (IPCC) to quantify global land air temperature change [*Hartmann et al.*, 2013].

2.4. CRUTEM4 Monthly Temperature Anomalies

CRUTEM4 (v4.4.0.0) is a monthly gridded temperature anomaly data set based on global all-sky station observations [*Jones et al.*, 2012]. The data set is produced through a collaborative effort between the Climatic Research Unit (CRU) at the University of East Anglia and the Met Office, both in the United Kingdom. Like GHCN-M, CRUTEM4 has been used by the IPCC to assess global land air temperature changes [*Hartmann et al.*, 2013]. It is an anomaly data set and represents a time series of mean monthly temperature anomalies with respect to the 1961–1990 baseline period at a spatial resolution of 5° latitude/longitude. CRUTEM4 data are used in the time series analysis presented in the second part of this study. The global time series of CRUTEM4 anomalies, which is also used in this part of the study, includes the 95% confidence intervals for uncertainty components that account for station and grid box sampling, coverage, and bias uncertainties (http://www.metoffice.gov.uk/hadobs/crutem4/data/diagnostics/time-series.html).

2.5. Other Data Sets Used in the Study

The LST-T_{2m} relationship is characterized with respect to land use, vegetation, and elevation. Land use classifications are sourced from the ESA Land Cover Climate Change Initiative (CCI) project version 1.6 data set (http://www.esa-landcover-cci.org/), which provides global maps at 300 m spatial resolution for three 5 year epochs: 1998–2002, 2003–2007, and 2008–2012 [*Bontemps et al.*, 2012; *Poulter et al.*, 2015]. The second epoch (2003–2007) was selected for this analysis to represent the mean land cover type over the analysis period (1995–2012). The CCI land cover types are given in Table 2.

For elevation, the Shuttle Radar Topography Mission (v1) data set was used [*Farr and Kobrick*, 2000; *Rodriguez et al.*, 2005]. This provides near-global land elevation at 30 m spatial resolution.

Table 2. Land Cover CCI Surface Types (see http://maps.elie.ucl.ac.be/CCI/viewer/index.php)[a]

Class	Legend Abbreviation	Description
10	Crops (rain)	Cropland, rainfed
20	Crops (irr.)	Cropland, irrigated/post flooding
30	Mos. Crop (>50%)	Mosaic cropland (>50%)/natural vegetation (tree, shrub, and herbaceous)
40	Mosaic nat.veg (>50%)	Mosaic natural vegetation (tree, shrub, and herbaceous cover) (>50%)
50	Broad. ever.	Tree cover, broadleaved, evergreen, closed to open (>15%)
60	Broad. decid.	Tree cover, broadleaved, deciduous, closed to open (>15%)
70	Need. ever.	Tree cover, needleleaved, evergreen, closed to open (>15%)
80	Need. decid.	Tree cover, needleleaved, deciduous, closed to open (>15%)
90	Mixed tree	Tree cover, mixed leaf type (broadleaved and needleleaved)
100	Mos. tree/shrub (>50%)	Mosaic tree and shrub (>50%)/herbaceous cover (<50%)
110	Mos. herb. (>50%)	Mosaic herbaceous cover (>50%)/tree and shrub (<50%)
120	Shrubland	Shrubland
130	Grassland	Grassland
140	Lich./mosses	Lichens and mosses
150	Sparse veg.	Sparse vegetation (tree, shrub, herbaceous cover) (<15%)
160	Tree, flood-fresh/brack.	Tree cover, flooded, fresh or brackish water
170	Tree, flood-saline	Tree cover, flooded, saline water
180	Shrub/herb. Flood.	Shrub or herbaceous cover, flooded, fresh/saline/brackish water
190	Urban	Urban areas
200	Bare areas	Bare areas
210	Water	Water bodies
220	Perm. snow/ice	Permanent snow and ice

[a]"Legend abbreviation" refers to the x axis labeling in Figure 8.

Fraction of vegetation data were sourced from the Copernicus Global land service (FCOVER v1.0), which provides near-global 10 day composites at 1/112° latitude/longitude [*Baret et al.*, 2013; *Camacho et al.* [2013].

Two additional LST data sets were used to verify the time series analysis in the second part of this study: MODIS monthly LST day and LST night fields at 0.05° latitude/longitude [*Wan*, 2013, 2014] and 6-hourly "skin" temperatures from the European Centre for Medium-Range Weather Forecasts Interim Reanalysis (ERA-Interim) [*Dee et al.*, 2011].

3. Methods

3.1. Analysis of the LST-T_{2m} Variability

The variability in the global LST-T_{2m} relationship is assessed by comparing the ATSR CDR with T_{2m} data from CRU TS and GHCN-M. CRU TS is used in preference to CRUTEM4 owing to its higher spatial resolution (recall that the ATSR CDR has spatial resolution of 0.05°) and availability of monthly averages of daily extreme temperatures (T_{min} and T_{max}). For the CRU TS comparisons, the CDR is reprojected onto a regular 0.5° grid separately for daytime and nighttime LSTs. For the GHCN-M comparisons, the CDR 0.05° cell nominally containing the station location is used. In both cases, LST_{day} is compared directly with T_{max} and LST_{night} with T_{min}.

Both the elevation and land use data sets are also resampled to 0.05 and 0.5° latitude/longitude. For elevation, the mean cell elevation is used. For land use, the dominant land cover class within each grid cell is assigned to the cell. Comparisons between the CDR and CRU TS are only performed for 0.5° cells where the percentage of LC CCI pixels within the cell matching the dominant land cover class is ≥80% and the fraction of water in the cell is ≤20%. Similarly, comparisons between the CDR and GHCN-M are only performed for 0.05° cells that also meet these criteria, and additionally, where the LC CCI classification of the GHCN-M station matches that of the CDR 0.05° cell. This is to ensure that the analysis is only carried out for cells and stations that truly represent the assigned land classification.

3.2. Comparison of LST and T_{2m} Time Series

The comparison between LST and T_{2m} time series is performed using the CRUTEM4 data set, which is widely used to study temporal changes in global T_{2m}. CRUTEM4 is a 5° latitude/longitude monthly mean anomaly data set referenced to the 1961–1990 baseline period, which is before the beginning of the ATSR CDR. To

facilitate like-with-like comparison, the ATSR CDR is first reprojected onto a 5° latitude/longitude grid before calculating a monthly mean LST from the average of the monthly LST_{day} and LST_{night} fields. This is then converted to a time series of monthly anomalies by subtracting a monthly mean LST climatology calculated over the August 1995 to March 2012 baseline period (excluding incomplete months in the CDR: see section 2.1). Monthly climatology values are only calculated for cells with at least 10 years of data. Since the mean T_{2m} has changed substantially between the two reference periods (1961–1990 and August 1995–March 2012) [*Hartmann et al.*, 2013], an "adjusted" version of the CRUTEM4 anomalies is also calculated by subtracting a monthly mean T_{2m} climatology of CRUTEM4 anomalies using the same ATSR CDR baseline period. The result is a time series of both ATSR CDR monthly mean LST anomalies and CRUTEM4 monthly mean T_{2m} anomalies, both referenced to the August 1995 to March 2012 baseline period.

The global mean time series for each 5° anomaly data set is calculated to be consistent with the averaging in CRUTEM4 time series presented by *Jones et al.* [2012]. Spatial averages are calculated separately for the northern (NH) and southern hemispheres (SH) by weighting each grid box by the cosine of its latitude [*Jones*, 1994]. The global mean value is then determined from (2NH + SH)/3, which approximates for the higher proportion of land in the NH [*Jones et al.*, 2012]. Two sets of comparisons are presented: a global time series where all available data from each data set are used, and a version that uses space-time cells where both data sets are present ("spatially matched"). The spatially matched version is included because both data sets contain gaps, which may introduce uncertainty into the comparison. The CRUTEM4 uncertainties (section 2.3) are included in the time series comparisons to indicate the likely range of monthly anomalies for this data set. The equivalent uncertainty envelope for the CDR is not presented as this cannot be determined from the uncertainty information provided in the version 1.0 data files. Retrieval uncertainties are propagated from the 1 km pixels through to the 0.05° CDR product, but further scaling is required to facilitate like-with-like comparison to CRUTEM4. Provision of independent uncertainty estimates in surface temperature retrieval from satellite data is subject of active research [*Bulgin et al.*, 2016] and as such, a rigorous methodology for propagating these uncertainties to provide an uncertainty envelope equivalent to CRUTEM4 is presently unavailable.

3.3. Statistical Parameters

The relationship between LST and T2 m is often explored in this study through the use of ordinary least squares regression. For example, T_{2m} (y axis) is plotted against LST (x axis)—a scatterplot—and the gradient of the linear regression line fitted to the data is reported in this study as the "slope." A slope of unity signifies that a 1°C change in T_{2m} equates to a 1°C change in LST, which would indicate that the two temperatures are perfectly coupled. The response of the LST-T_{2m} difference (y axis) with other parameters, e.g., vegetation fraction (x axis), is explored in the same way. Here the reported slope is the gradient of the linear regression line fitted to these data. P values for reported correlations and slopes are calculated using a two-tailed student T test with P values above 0.05 considered here to indicate a result that is likely to have occurred by chance and is therefore insignificant.

In the second part of this study, differences in the rate of change in LST and T_{2m} over the 1995–2012 period are assessed by calculating the trend in the LST-T_{2m} difference time series. For this analysis, the median of pairwise slopes [*Sen*, 1968] is used to calculate the trend; the 95% confidence interval on the trend is also given. Where this interval does not encompass zero, it is assumed that there is high confidence that the calculated trend is nonzero.

4. Results Part 1: Assessment of the LST-T_{2m} Variability

4.1. Spatial Variation in the Relationship Between LST and T_{2m}

Figures 3 and 4 show global maps of the mean monthly temperatures for CRU TS and the CDR averaged over all occurrences of December/January/February (DJF), March/April/May (MAM), June/July/August (JJA), and September/October/November (SON) from August 1995 through March 2012. Figure 3 shows the side-by-side comparisons for T_{min} and LST_{night}, while Figure 4 shows T_{max} and LST_{day}. The CDR minus CRU TS differences are shown in Figure 5. Figure 6 presents the normalized frequency distributions of the temperature differences, based on the full time series of data.
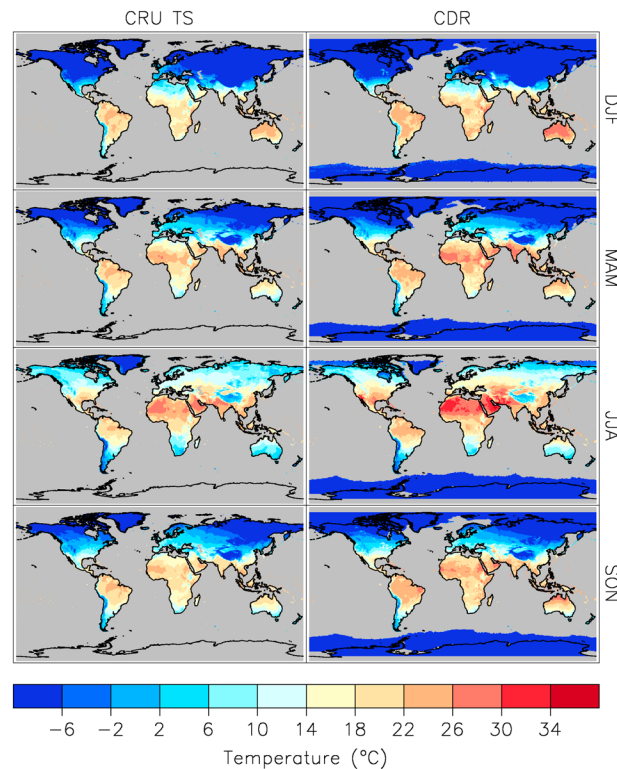
Figure 3. Seasonal mean temperatures from (left) the CRU TS v3.23 T_{min} and (right) the CDR LST night for December/January/February (DJF), March/April/May (MAM), June/July/August (JJA), and September/October/November (SON). Seasonal means are calculated from data acquired August 1995 through March 2012 (excluding January–June 1996 and January–June 2001, which are incomplete months in the CDR; see text).

In general, the spatial patterns exhibited by both sets of data are very similar, with CRU TS and the CDR showing the same dominant features. LST_{night} and T_{min} are generally within ±5°C, although LST_{night} is typically warmer than T_{min}, with median difference for the globe for all seasons of 1.8°C (Figure 6a). This is expected because the nominal night observation time for the CDR is 10:00 P.M. when LST would still be warmer than T_{min}, which typically occurs close to sunrise [*Edwards et al.*, 2011; *Good*, 2016; *Jin et al.*, 1997]. However, there are notable situations where LST_{night} is cooler than T_{min}, for example, in Europe and Russia in DJF and SON (Figure 5, left). For the mid-high-latitude winter, colder LST_{night} could be due to snow cover [*Good*, 2016] or the clear-sky sampling bias of LST_{night} on cold, clear winter nights when surface is cooling more efficiently compared with cloudy nights. LST_{night} and T_{min} are most similar over tropical vegetated regions— the role of vegetation is explored further in the following sections.

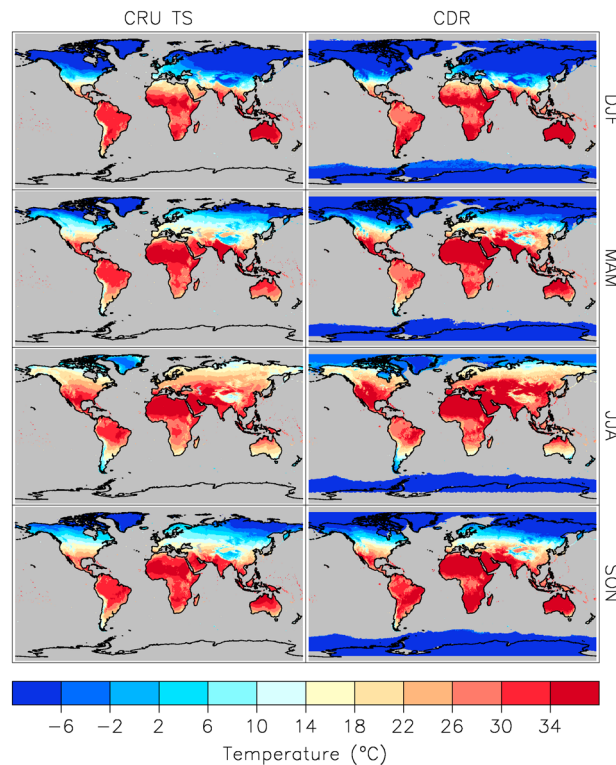The differences between LST_{day} and T_{max} are larger in magnitude with a high degree of spatial variability, although the median global LST_{day}-T_{max} difference for all seasons is −0.1°C (Figure 6b). LST_{day} is typically cooler than T_{max} at very high latitudes, over some equatorial regions in all seasons, and at middle latitudes during winter (Figure 5, right). These spatial patterns are very similar to those reported by *Lian et al.* [2017], who analyzed differences between MODIS/Aqua maximum monthly LSTs and T_{max} from CRU-TS. The tendency of LST_{day} to fall below T_{max} at high latitudes and during winter months can be explained by the lower insolation in these regimes resulting in cold LSTs, whereas T_{2m} is higher because the air has passed over warmer SSTs. LSTs that are colder than T_{2m} may also occur over snow-covered surfaces. Negative LST-T_{2m} differences over equatorial regions have been reported previously by *Jin et al.* [1997], who analyze modeled LST and T_{2m}; this is discussed further in section 4.2. *Jin et al.* [1997] also observed cooler LSTs compared with T_{2m} in winter at middle-to-high latitudes in their simulations.

By contrast, LST_{day} tends to be warmer than T_{max} over the dry tropics in all seasons and at middle latitudes during the summer months. This positive difference occurs because at the 10:00 A.M. nominal observation time of the CDR, the clear-sky insolation in these regimes is high enough to elevate LST above T_{2m} by several degrees, and even above T_{max} [*Edwards et al.*, 2011; *Good*, 2016; *Jin et al.*, 1997]. The results for the same analysis using GHCN-M station data illustrate the same general features (not shown).

The distributions of differences shown in Figure 6 include comparisons between the CDR LSTs and T_{mean}. This indicates that in both cases, closer agreement in magnitude is obtained between LST_{night} and T_{min}, and LST_{day} and T_{max}, than the equivalent comparisons with T_{mean}. Both the LST_{night}-T_{min} and LST_{night}-T_{mean} distributions are approximately Gaussian.

Figure 7 shows the CRU TS versus CDR linear regression slopes (see section 3.3) and correlation coefficients for each 0.5° cell, for the complete >17 year time series. Slopes close to unity indicate situations where a 1°C

Figure 4. As for Figure 3 but for (left) the CRU TS v3.23 T_{max} and (right) the CDR LST day.

change in LST corresponds to a 1°C change in T_{2m}. Thus, areas where both the correlation and slope are close to unity correspond to where LST and T_{2m} are generally well coupled. This is observed for LST_{night}/T_{min} for much of the middle-to-high latitudes and for LST_{day}/T_{max} in parts of north-east Asia. Elsewhere, slopes are generally <0.8 although correlation coefficients still nearly always exceed 0.9 outside of the tropics. This indicates that LST becomes increasingly warmer than T_{2m} with increasing temperature. For both LST_{night}/T_{min} and LST_{day}/T_{max}, the correlations and slopes are substantially lower over the equatorial regions, with a marked latitudinal gradient in correlation toward the equator in both hemispheres. This is consistent with the results of *Jin et al.* [1997] who also found lower LST-T_{2m} correlations in model simulations at lower latitudes compared with middle-to-high latitudes.

Both the T_{min} versus LST_{night} and T_{max} versus LST_{day} slopes tend to be less than unity, indicating that the LST-T_{2m} difference becomes more positive with increasing temperatures. This pattern has been noted previously by *Mildrexler et al.* [2011], who reported an increasing difference between annual maximum LST and T_{2m} with increasing temperature. While the deviation from unity for T_{min}/LST_{night} in this study is reasonably small (usually within the range 0.8–1.1), the T_{max}/LST_{day} slope is typically less than 0.7. This is consistent with the more extreme range of $LST_{day}-T_{max}$ differences observed in Figure 5.

4.2. Variability in LST-T_{2m} Differences by Land Cover Classification

Figure 8 shows the characteristics of the CDR-CRUT TS relationship as a function of land cover classification. The positive $LST_{night}-T_{min}$ difference and slope of slightly less than unity reported in section 4.1 seems reasonably consistent across all surface types (Figures 8a and 8b). The proximity of the slopes to unity—all but one are between 0.88 and 1.1—and high correlation coefficients (Figure 8c) indicate a close coupling between LST_{night} and T_{min} for most land cover types, which is consistent with the maps in section 4.1 and with findings reported in previous studies examining the LST-T_{2m} relationship [e.g., *Good*, 2016, *Zhang et al.*, 2011].

As inferred from Figures 4–7, the relationship between LST_{day} and T_{max} is more complex and dependent on surface regime. The variability in $LST_{day}-T_{max}$, both within and between surface types, is much higher than for $LST_{night}-T_{min}$ (Figure 8a), also indicated by the slightly lower correlation coefficients (Figure 8c). The slope of the T_{max} versus LST_{day} relationship is lower than for T_{min} versus LST_{night} (Figure 8b), reflecting the dependence of LST on insolation, increasing the $LST_{day}-T_{max}$ difference at higher solar elevations, and therefore at higher surface temperatures. A notable feature of Figure 8 is that the $LST_{day}-T_{max}$ difference tends to be negative over the forested land cover types (classes 50–80), which by definition represent some of the more vegetated surfaces. Healthy vegetation actively transpires, losing surface heat to the overlying atmosphere [*Sun et al.*, 2015], thus reducing LST relative to T_{2m}. Greater surface roughness over vegetation also increases turbulent mixing, which also aids transfer of heat from the surface to the overlying air. Cooler LSTs are generally associated with increased vegetation density, and LST and T_{2m} are often close in areas of dense vegetation [*Jin and Dickinson*, 2010; *Mildrexler et al.*, 2011]. Negative $LST_{day}-T_{max}$ differences are also characteristic
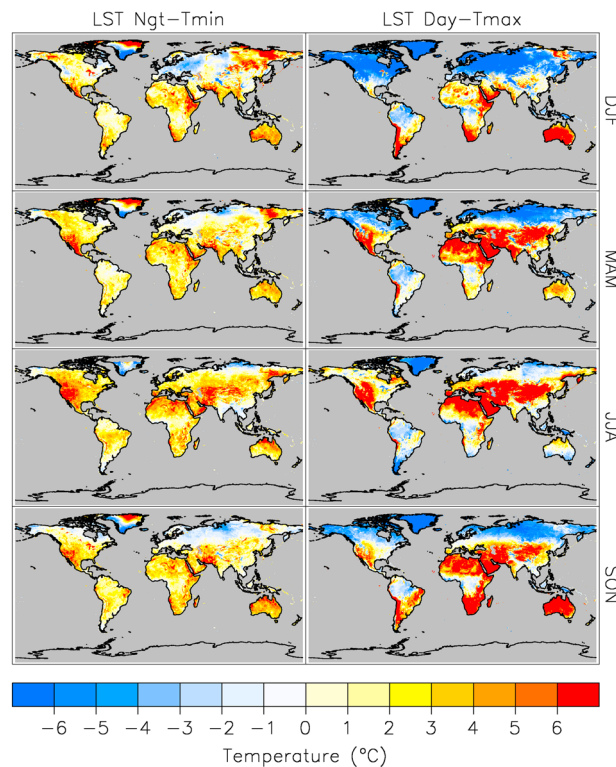
Figure 5. (left) CDR LST night minus CRU TS v3.23 T_{min} differences and (right) CDR LST day minus CRU TS v3.23 T_{max} differences for December/January/February (DJF), March/April/May (MAM), June/July/August (JJA), and September/October/November (SON). Seasonal means are calculated from data acquired August 1995 through March 2012.

of the lichens and mosses and permanent snow and ice classes, which occur at high latitudes and therefore lower solar elevation and colder LSTs. Positive LST_{day}-T_{max} differences, on the other hand, occur over shrubland, grassland, and bare area classes. The bare area class in particular is associated with low latitudes, where the high insolation and lack of vegetation can result in extremely high LSTs that are well above T_{max}, even at 10 A.M. local time [e.g., see *Good*, 2016] (Figure 1).

The same analysis using GHCN-M stations in place of CRU TS presents very similar results (not shown), although the number of land cover types represented is lower. Usefully, this finer-scale analysis enables the comparison of LST and T_{2m} over urban areas, which was not possible at the 0.5° spatial scale of CRU TS. For this surface type, based on 394 stations, a median difference of 2.1°C (interquartile range: 4.1°C) for LST_{night} minus T_{min} and 3.0°C (interquartile range: 6.7°C) for LST_{day} minus T_{max} is obtained. The nature of the relationship over this surface, and its similarity to some of the less vegetated classes, is expected given that urban areas are often very sparsely vegetated. However, it should be noted that turbulent fluxes are likely to be more efficient coupling T_{2m} and LST over urban areas owing to increased surface roughness in this regime compared with sparsely vegetated surfaces [*Stull*, 2015, pg 700]. There is a weak dependence of the urban LST-T_{2m} relationship with latitude (not shown), where the sign of the differences becomes slightly more negative, and the variability increases toward the higher latitudes, probably reflecting the variation in insolation with latitude.

Both the GHCN-M and CRU TS analyses suggest substantially lower correlations and slopes between LST and T_{2m} over the broadleaved evergreen tree cover class (class 50). This class represents the equatorial forests and is spatially consistent with the low-correlation/low-slope regions evident in Figure 7. Although LST and T_{2m} tend to be close in these areas (Figure 5 and also see *Mildrexler et al.* [2011]), the temperatures are poorly correlated because the diurnal range of both LSTs and T_{2m} is typically small with little seasonality [*Good*, 2016; *Jin and Dickinson*, 2010]. The influence of vegetation on the LST-T_{2m} relationship is discussed further in the following section.

4.3. Variability in LST-T_{2m} Differences With Vegetation Fraction

Figure 9 shows the variation in LST-T_{2m} difference with vegetation fraction for different ranges of SZA at solar noon. While the presentation of the results approximates high-to-low latitude from top to bottom, SZA was used to partition the results so that seasonal variability is also taken into account.

The general pattern of results is consistent with, e.g., *Mildrexler et al.* [2011], indicating that LST and T_{2m} become increasingly close with increasing fractional vegetation cover (FVC). Over full vegetation cover (FVC = 1) the difference between them tends to be a degree or so above zero for LST_{night}/T_{min} except at SZAs ≥65° and a few degrees below zero for LST_{day}/T_{max}. (The y intercept for full vegetation cover is simply the sum of the intercept and 10 times the slope since the maximum value of FVC is 1.) For both temperature pairs, the intercept becomes increasingly positive and the slope becomes increasingly negative (except for
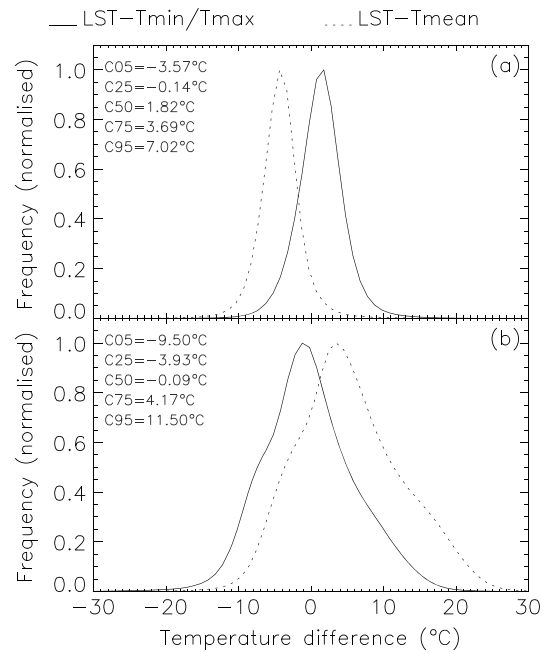
Figure 6. Normalized distributions of the CDR minus CRU TS differences for (a) LST_{night}-T_{min} (solid line) and LST_{night}-T_{mean} (dotted line) and (b) LST_{day}-T_{max} (solid line) and LST_{day}-T_{mean} (dotted line). The histograms are calculated from data acquired August 1995 through March 2012. The 5th (C05), 25th (C25), 50th (C50), 75th (C75,) and 95th (C95) centiles of the LST_{night}-T_{min} (Figure 6a) and LST_{day}-T_{max} (Figure 6b) differences are shown on each panel.

LST_{night}/T_{min} for SZA ≥65°) with decreasing SZA. This is more marked for the LST_{day}/T_{max} analysis compared with LST_{night}/T_{min}, again indicating the dependency of LST on insolation. The results suggest that for well-vegetated surfaces (e.g., FVC > 0.8), LST_{night}/LST_{day} may provide a reasonable proxy for T_{min}/T_{max} for all ranges of SZA for some applications. For regimes where the SZA is above 45°, T_{min}/T_{max} is reasonably well approximated by LST_{night}/LST_{day} except for sparsely vegetated and bare surfaces (e.g., FVC < 0.2).
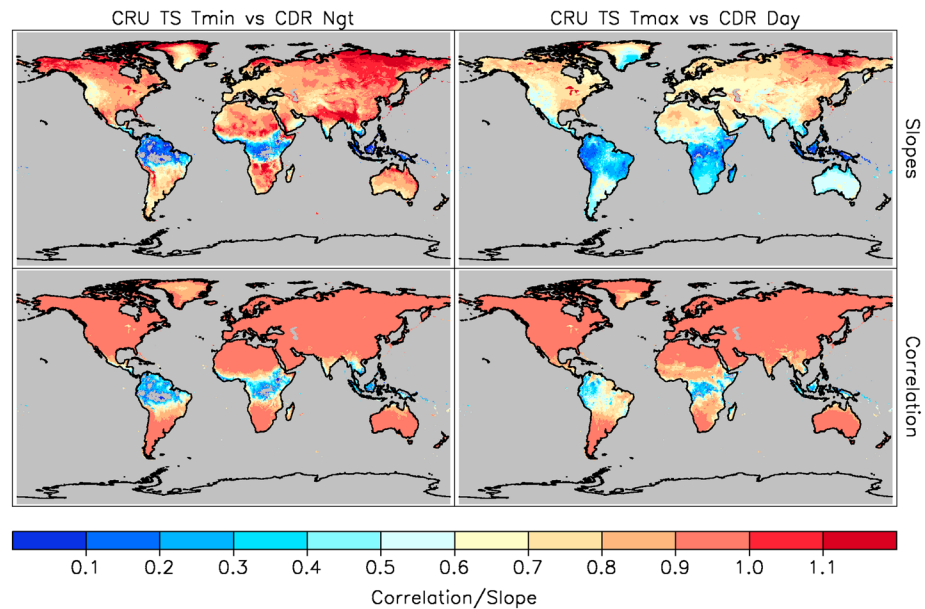

Figure 7. Maps showing spatial variability in the LST-T_{2m} relationship. (left column) The T_{min} versus LST night relationship and (right column) T_{max} versus LST day. (top row) The slopes (regression of T_{2m} as a function of LST) and (bottom row) correlation coefficients are plotted for each 0.5° grid cell. Correlations/slopes where the P value is >0.05 are excluded from the maps (gray). There are no negative slopes/correlation coefficients.
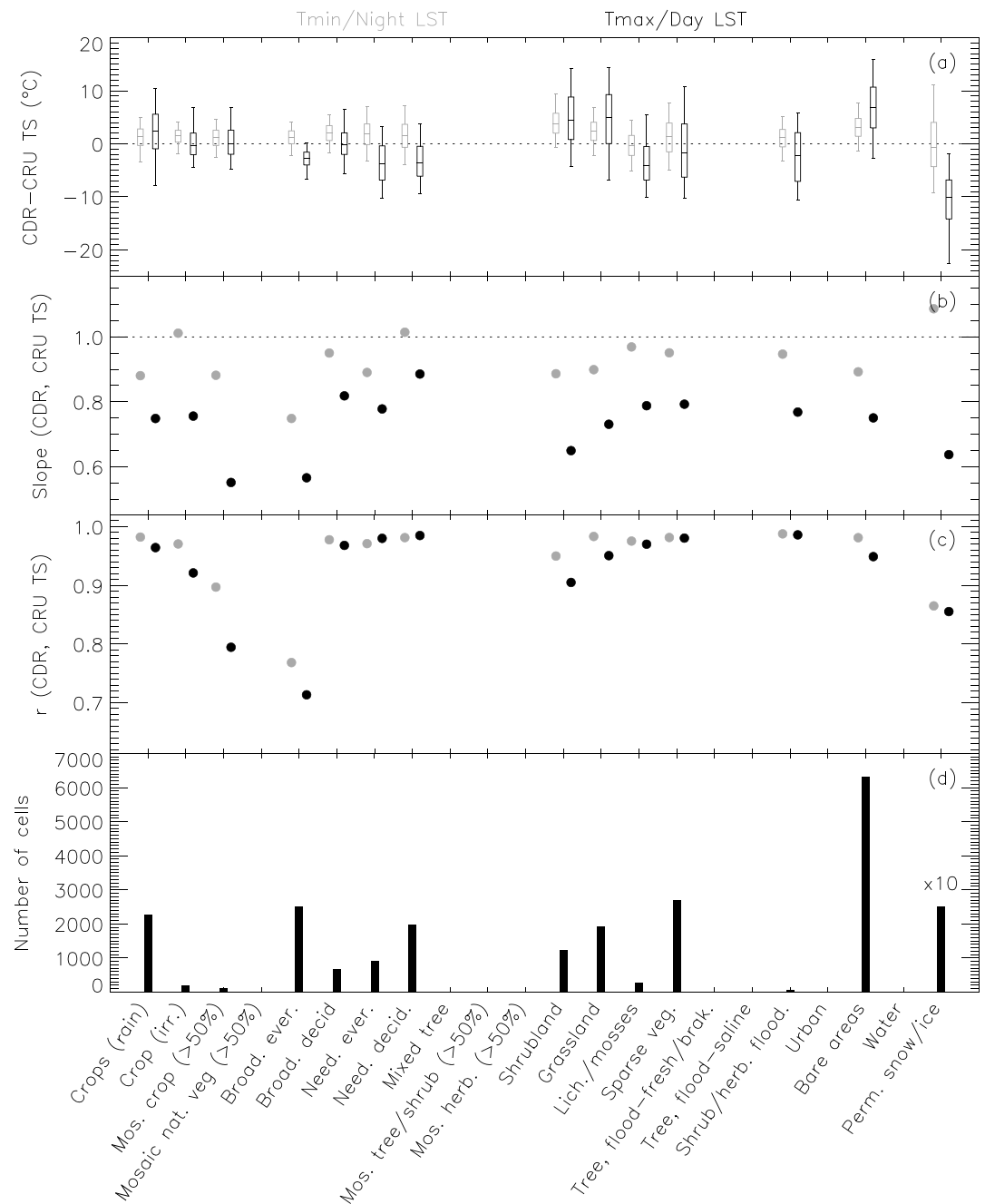
Figure 8. Characteristics of the differences between temporally and spatially collocated CDR and CRU TS observations by land cover type, where the dominant land cover class is present in ≥80% of the grid cell. The x axis indicates the land cover class (Table 2). (a) The 5/95th centiles (whiskers), 25/75th centiles (box), and median (horizontal line within the box) CDR-CRU TS difference; (b) the slope of the CRU versus CDR relationship; (c) the correlation coefficient; and (d) the number of grid cells analyzed. Matchups where the fraction of water in the grid cell is >20% have been excluded from the analysis. All correlations/slopes have a P value ≤0.05. Note that the number of stations for the permanent snow or ice land cover class has been reduced by a scaling factor of 10 (multiply bar by 10 for correct number).

4.4. Variability in LST-T_{2m} Differences by Elevation

Figure 10 illustrates the variation in LST-T_{2m} relationship with elevation, which has received little attention in previous studies. LST_{night}-T_{min} differences appear to be quite stable, while LST_{day}-T_{max} differences have a general tendency to increase with increasing elevation. For both temperature comparisons, there is a clear decrease in both the slope and correlation coefficient with increasing elevation indicating a de-coupling of
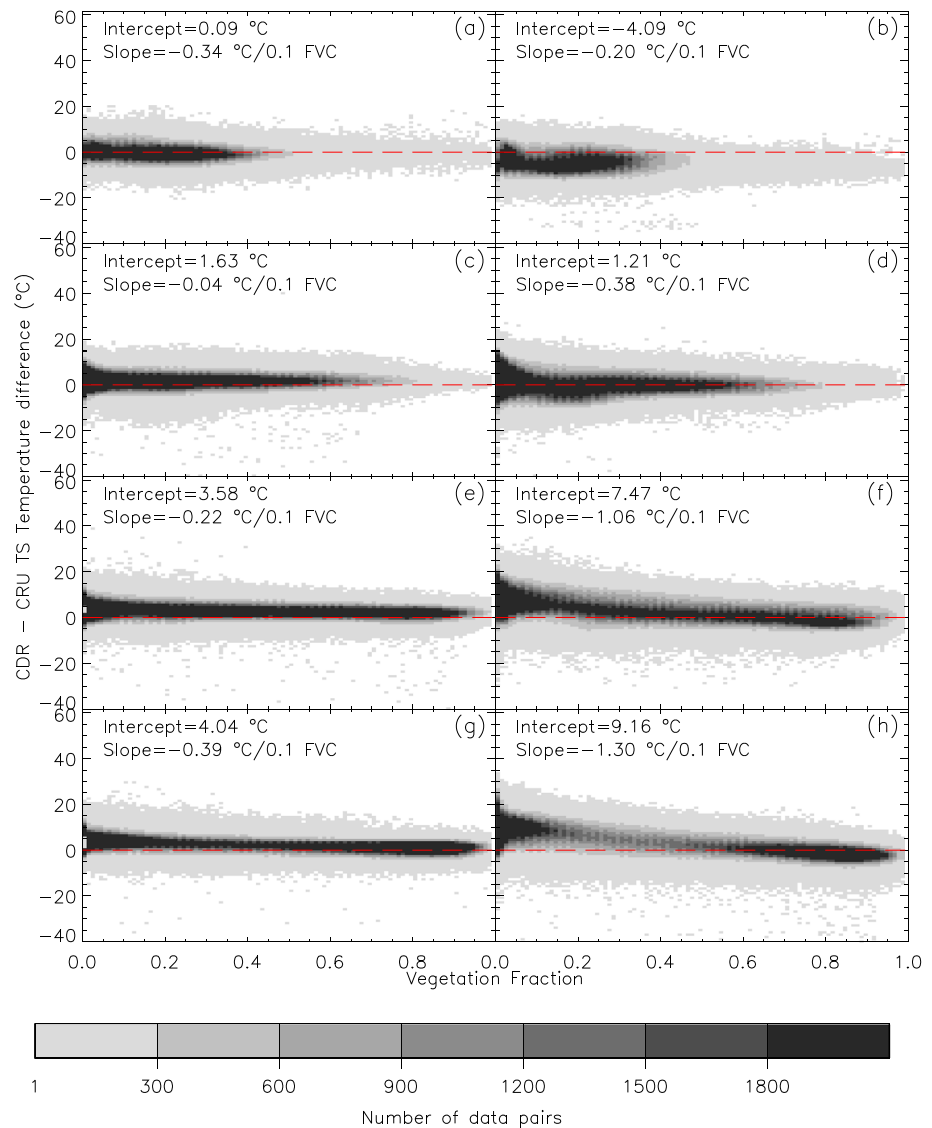
Figure 9. Variation in CDR minus CRU TS differences with vegetation fraction, for (a) LST_{night}-T_{min} and (b) LST_{day}-T_{max} for SZA > 65° (i.e., high latitudes), (c) LST_{night}-T_{min} and (d) LST_{day}-T_{max} for 45° ≥ SZA < 65°, (e) LST_{night}-T_{min} and (f) LST_{day}-T_{max} for 20° ≥ SZA < 45°, and (g) LST_{night}-T_{min} and (h) LST_{day}-T_{max} for SZA < 20° (i.e., low latitudes). "SZA" refers to the SZA value at solar noon—see text.

the LST-T_{2m} relationship at altitude. The effect is more marked for the LST_{day}-T_{max} comparison. This may, at least in part, be due to the fact that all-sky T_{2m} are being compared with clear-sky LSTs. However, at high altitude, it is possible for LST to be elevated by heat from the Sun, while T_{2m} may be cooler because of the temperature lapse rate and exchange with the surrounding free air. This was also noted by *Good* [2016], who analyzed ground-based observations of all-sky LST and T_{2m} at 19 of the Atmospheric Radiation Measurement program sites, including two at high elevations. The equivalent analysis using GHCN-D stations demonstrates very similar results (not shown), although the dropoff in correlation with increasing elevation is perhaps slightly less apparent, which probably reflects the lack of very high-altitude stations.

5. Results Part 2: Comparison of LST and T_{2m} Time Series

5.1. Spatially Averaged Time Series Comparisons

The time series of CDR monthly mean anomalies is shown in Figure 11a, together with the equivalent time series from CRUTEM4. The CRUTEM4 global time series is provided with lower and upper 95% confidence
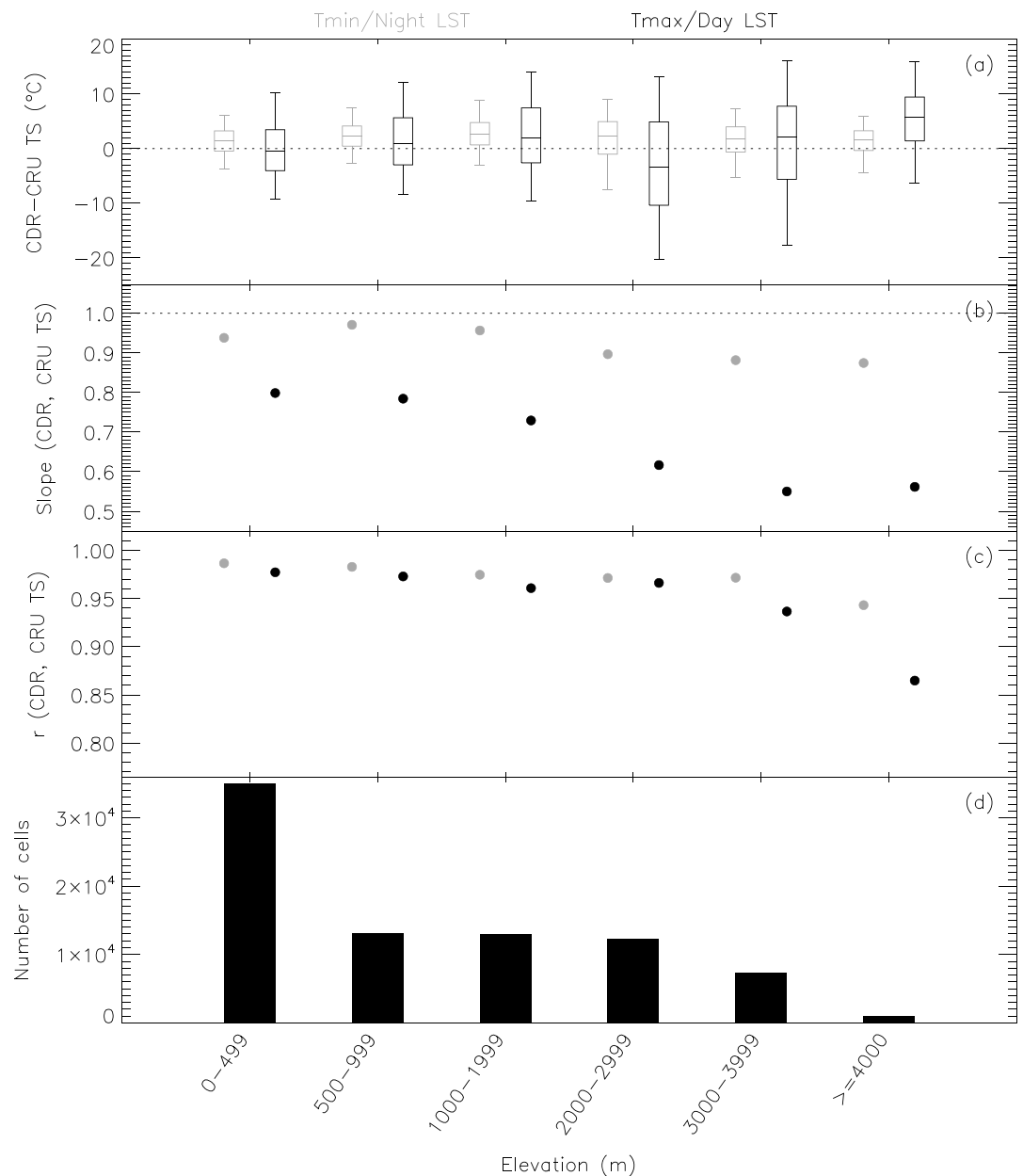
Figure 10. As Figure 8 except showing the variation in the LST-T_{2m} relationship with elevation. The x axis shows the elevation range of the data plotted (in meters).

intervals, which are displayed as shading on the plot. The CDR and CRUTEM4 time series show remarkable agreement, with the ATSR CDR providing useful independent verification of the CRUTEM global monthly T_{2m} anomaly time series. The correlation between the adjusted CRUTEM4 time series (i.e., referenced to August 1995 to March 2012 baseline) and the CDR is 0.76 ($p < 0.01$), with 166 of the 188 CDR data points (88%) falling within the CRUTEM4 uncertainties (blue shading in Figure 11).

Both data sets suffer from spatial gaps. For example, much of Africa and Antarctica are regularly missing from CRUTEM4, while the ATSR data set does not provide monthly observations under persistent cloud. With this in mind, Figure 11b shows the same time series but for global averages using only cells where both data sets have observations in that month. The correlation increases to 0.87 ($p < 0.01$) for this spatially matched time series.

The difference between the time series of anomalies is shown in Figure 11c. The linear trend of this differenced time series is negative (e.g., -0.17°C/decade for the spatially matched comparison, 95% confidence
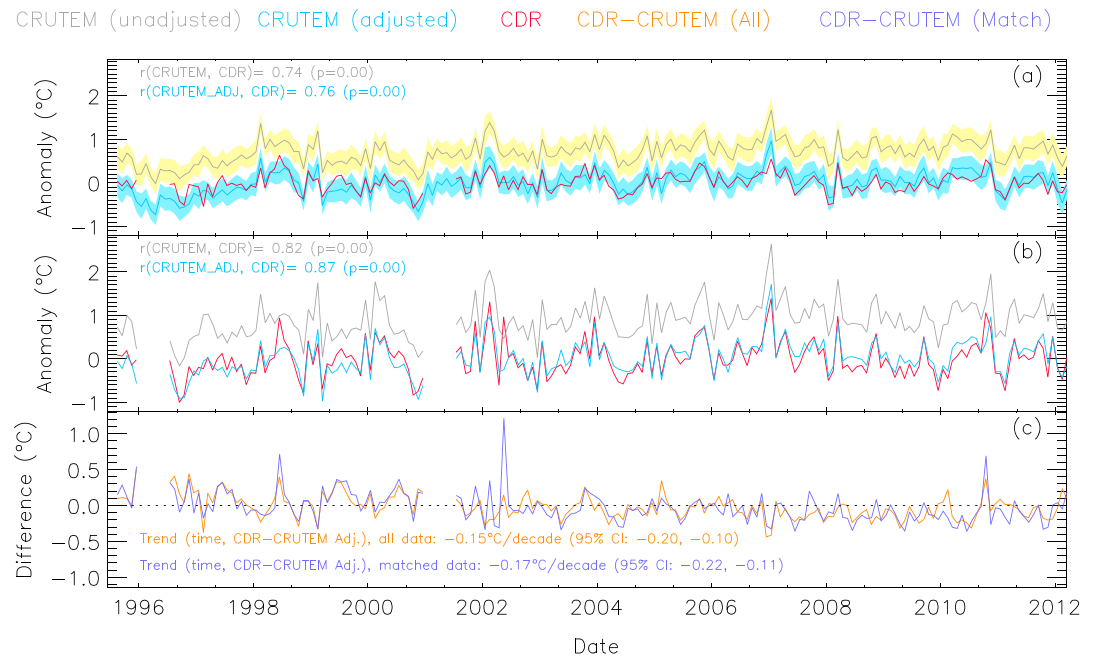
Figure 11. Time series of globally averaged monthly anomalies (°C) for the CDR and CRUTEM4 data set. The results for the "unadjusted" CRUTEM4 data correspond to the original CRUTEM4 anomalies (baseline 1961–1990). The "adjusted" CRUTEM4 data are the anomalies referenced to the August 1995 to March 2012 baseline period. The CDR anomalies are also referenced to this period. (a) Averages using all available data points for each data set. (b) Averages using only cells where both data sets are present. (c) The respective CDR minus CRUTEM4 differences where all corresponds to the data shown in Figure 11a and "Match" to the data shown in Figure 11b. The 95% confidence interval for the difference trends are indicated on the plot. The shading represents the total uncertainties associated with the CRUTEM4 time series (sourced from http://www.metoffice.gov.uk/hadobs/crutem4/data/diagnostics/index.html).

range − 0.22 to −0.11), implying that the two data sets may not exhibit the same rate of temperature change with time. While this apparent difference might seem surprising, it should be regarded with caution given the short time series (<18 years). This analysis uses version 1.0 of the ATSR CDR, and part of the motivation of this study is to assess the temporal consistency of the time series, particularly as there may be residual inhomogeneities caused by the transition from ATSR-2 to AATSR, for example, due to the change in overpass time of the sensors (as discussed in later sections).

5.1.1. Analysis of the CDR-CRUTEM4 Differenced Time Series

Figure 11 suggests that the ATSR-2 portion of the time series, which ends in April 2002, is noisier and the CDR-CRUTEM4 differences more positive compared with those of the AATSR (from May 2002). Figure 12 shows the median CDR minus CRUTEM4 anomaly differences, for the whole time series, by season and by sensor. Results are shown for the globe and for different geographical regions (Table 3). For nearly all regions, the CDR-CRUTEM4 differences are clearly more positive for ATSR-2 compared with AATSR; for the globe (spatially matched cells), the median CDR minus CRUTEM4 difference is 0.07°C for ATSR-2 and −0.10°C for AATSR. This could account for the overall negative trend in the CDR-CRUTEM4 time series, since ATSR-2 preceded AATSR. The median difference for the whole series for most regions is slightly negative, reflecting the longer AATSR record. There is some seasonal variation in the median differences, although no clear pattern is evident, other than perhaps an increased clustering of the differences around zero in DJF and SON.

Figure 13 shows similar graphics but for the trends of the CDR minus CRUTEM4 time series; in this case, trends that are not statistically different from zero (see section 3.3) are indicated by an unfilled symbol. Table 3 provides the numerical values of the trends for the whole time series, together with the correlation coefficients between the CDR and CRUTEM4 time series for each region. For the spatially matched comparisons, all regions with significant trends (i.e., not statistically different from zero) for mean LST are negative although the magnitude is variable, ranging between −0.43 (South Asia) to −0.17 (Globe) °C/decade. When considering the sensor-partitioned results, there are some small differences between the trends, with the ATSR-2 time series trends tending to be slightly more negative than AATSR. However, the confidence in these results is
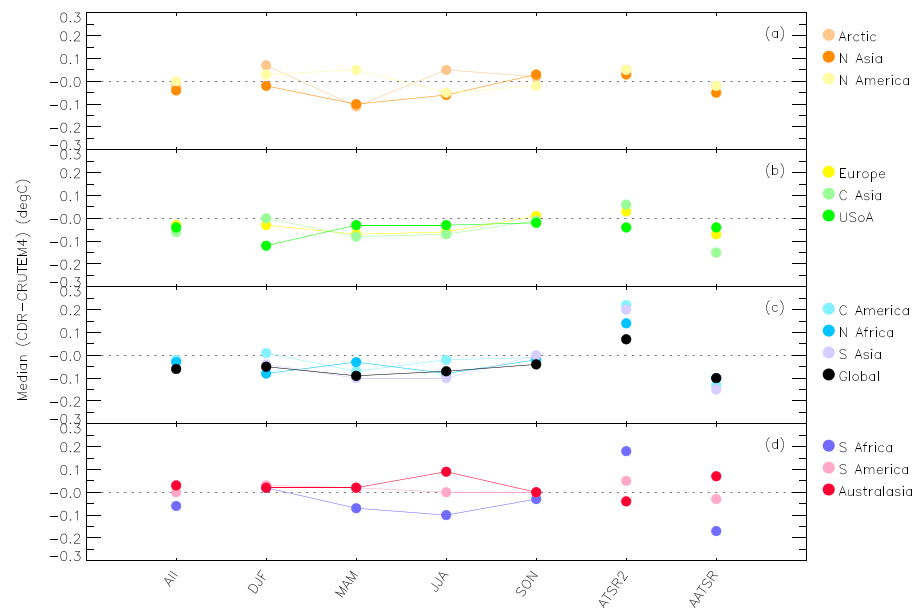
Figure 12. Summary of the median CDR minus CRUTEM4 anomaly differences for regions with central latitude (a) 60–90°N, (b) 30–60°N, (c) 0–30°N, and (d) −30 to 0°N. Results are shown for all seasons and sensors (all), by season (DJF/MAM/JJA/SON), and by sensor (ATSR2 and AATSR). The results are for spatially matched grids only. Antarctica is excluded from the analysis owing to the very small number of data points in this region.

lower than for the full time series given the even shorter record length (<10 years), as emphasized by the large number of regional trends that are not statistically different from zero (unfilled symbols in Figure 13).

The evidence presented in Figures 11–13 suggests that there may be some discrepancy between the ATSR-2 and AATSR portions of the CDR. A likely source of this discrepancy is in the overpass time correction that is applied to the ATSR-2 CDR LSTs to align them with the AATSR overpass, which is 30 min earlier (section 2.1). LST can change by several °C in 30 min particularly around the 10 A.M. nominal overpass time of the CDR [*Good*, 2016; *Jin and Dickinson*, 2010]; thus, this correction is likely to introduce errors into the ATSR-2 LSTs. These errors could be the cause of the variation in the median CDR-CRUTEM4 anomaly difference between ATSR-2 and AATSR (Figure 12) and the apparently higher noise in the ATSR-2 portion of the time series (Figure 11c).

Table 3. Relationships Between Time Series of Anomalies From CRUTEM4 (Adjusted to 1995–2012 Baseline) and the CDR[a]

Region Name	Min Lat	Max Lat	Min Lon	Max Lon	R (All Data)		R (Spatially Matched)		Trend (All Data) (°C/Decade)		Trend (Spatially Matched) (°C/Decade)	
					Mean	Night	Mean	Night	Mean	Night	Mean	Night
Globe	−90	90	−180	180	0.76	0.83	0.87	0.90	−0.15	(−0.02)	−0.17	−0.08
Europe	30	70	−15	40	0.95	0.95	0.95	0.96	−0.10	−0.06	(−0.08)	(−0.05)
North America	50	70	−170	−50	0.94	0.94	0.94	0.94	(−0.12)	(−0.08)	−0.17	−0.11
USA	30	50	−130	−50	0.93	0.93	0.93	0.93	(−0.04)	(−0.06)	−0.05	−0.05
Central America	10	30	−130	−60	0.69	0.82	0.71	0.83	−0.27	−0.10	−0.25	−0.09
South America	−60	10	−85	−30	0.76	0.85	0.77	0.86	−0.10	(0.01)	(−0.05)	(0.00)
North Africa	0	30	−20	60	0.78	0.88	0.77	0.89	−0.26	−0.15	−0.24	−0.14
South Africa	−40	0	−20	60	0.58	0.77	0.58	0.76	−0.34	−0.08	−0.32	(−0.04)
Australasia	−50	−10	110	180	0.76	0.80	0.78	0.85	−0.15	(−0.03)	(−0.10)	(0.01)
South Asia	−15	30	60	155	0.56	0.81	0.70	0.87	−0.49	−0.14	−0.43	−0.12
Central Asia	30	50	40	145	0.93	0.95	0.93	0.95	−0.25	−0.12	−0.22	−0.11
North Asia	50	70	40	180	0.94	0.95	0.95	0.96	(0.06)	(0.03)	(0.03)	(0.03)
Arctic	70	90	−180	180	0.82	0.84	0.90	0.93	(−0.22)	(−0.18)	(−0.14)	−0.24

[a]"Trend" indicates the trend of the differenced time series (CDR minus CRUTEM4) with time. Results are for spatially averaged time series using all grid cells available for each data set ("all data") and only grid cells that are available in both data sets (spatially matched), and separately using the mean LST time series ("mean"), and LST_night only ("night"). Results in brackets indicate trends that are not statistically different from zero (see section 3.3). Antarctica is excluded from the analysis owing to the very small number of data points in this region. R is the correlation coefficient.
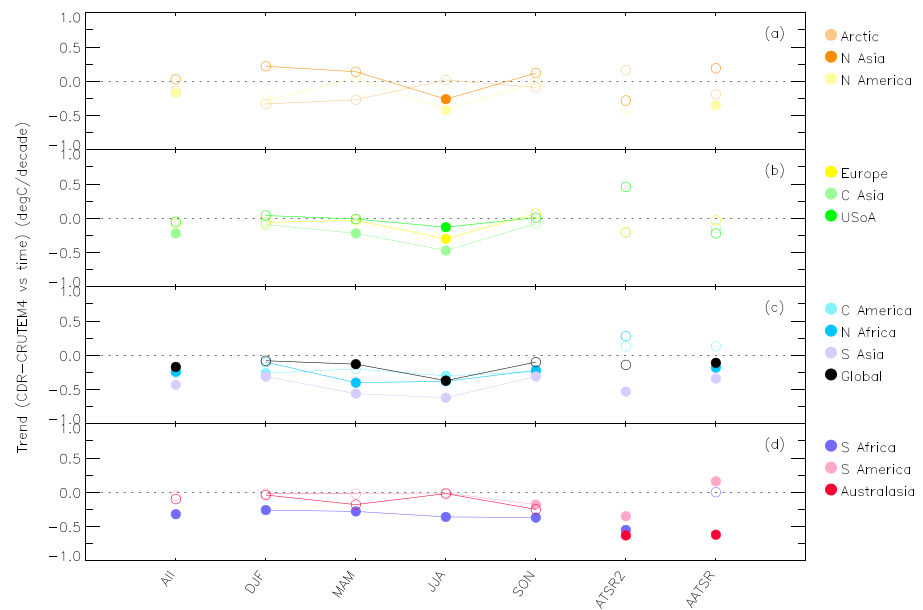
Figure 13. As for Figure 12 but showing the trend of the CDR minus CRUTEM4 time series. Results denoted by an unfilled symbol indicate where trends are not statistically different from zero.

The uncertainty in the ATSR-2 CDR LST temporal correction will naturally be larger where insolation is higher, especially where vegetation cover is low, as this is where LST changes most rapidly. While there was no clear pattern in the seasonal median differences (Figure 12), there does appear to be a tendency of the JJA trends in the NH regions to be slightly more negative (Figures 13a–13c). For the lower latitude NH regions (Figure 13c), this tendency also appears in MAM. If these more negative trends correspond to more warm-biased ATSR-2 anomalies, this would support the hypothesis that the ATSR-2 LST temporal correction is at least partly responsible for the relative lack of warming in the CDR compared with CRUTEM4, as this is also consistent with regimes with higher insolation, and therefore potentially larger errors in the LST temporal correction.

To verify that the negative CDR minus CRUTEM4 trends are a result of inhomogeneities in the ATSR CDR rather than an actual difference in rate of temperature change in the two data sets, the analysis presented in Figures 12 and 13 has been repeated using ERA-Interim reanalysis skin temperatures in place of CRUTEM4. ERA-Interim does not assimilate satellite LST data so the CDR and ERA-Interim are independent. To do this, the ERA-Interim data were aggregated from 6-hourly instantaneous skin temperatures to monthly mean anomalies, relative to the same baseline period (August 1995 to March 2012). The results are remarkably similar to the analysis using CRUTEM4 (not shown). The correlation between the CDR and ERA-Interim anomalies is high ($r = 0.81$, $p < 0.01$), with a median difference across the whole time series of $-0.01°C$ and a root-mean-square difference of $0.20°C$. The median global anomaly difference is positive for the ATSR-2 portion of the CDR ($0.03°C$) and negative for the AATSR portion ($-0.06°C$), while the linear trend of the CDR minus ERA Interim time series is $-0.11°C/decade$ (confidence interval: -0.16 to -0.06). The trend for the global ATSR-2 CDR minus ERA Interim difference is -0.30 (confidence interval: -1.25 to -0.80), while for the AATSR CDR-ERA Interim, no significant trend is detected ($0.06°C/decade$, confidence interval: -0.05 to 0.17).

The similarity between the CDR-CRUTEM4 and CDR-ERA-Interim comparisons strongly suggests that while the month-to-month variability in anomalies between the three data sets is in remarkably close agreement, the CDR v1.0 contains some nonclimatic artifacts. Performing the same analysis using MODIS-Terra LSTs is less informative regarding the stability of the ATSR-2/AATSR transition (not shown) because this comparison includes only 21 months of ATSR-2 data from the CDR. For the global analysis, none of the mean monthly CDR minus MODIS trends are statistically different from zero, which suggests that the CDR (mostly AATSR) and MODIS generally agree on the rate of change of LST between February 2000 and March 2012.

The results reported above analyze the mean monthly CDR LST, which is calculated from an average of LST_{day} and LST_{night}. A comparison with GHCN-M, which provides temporally homogeneous station-based

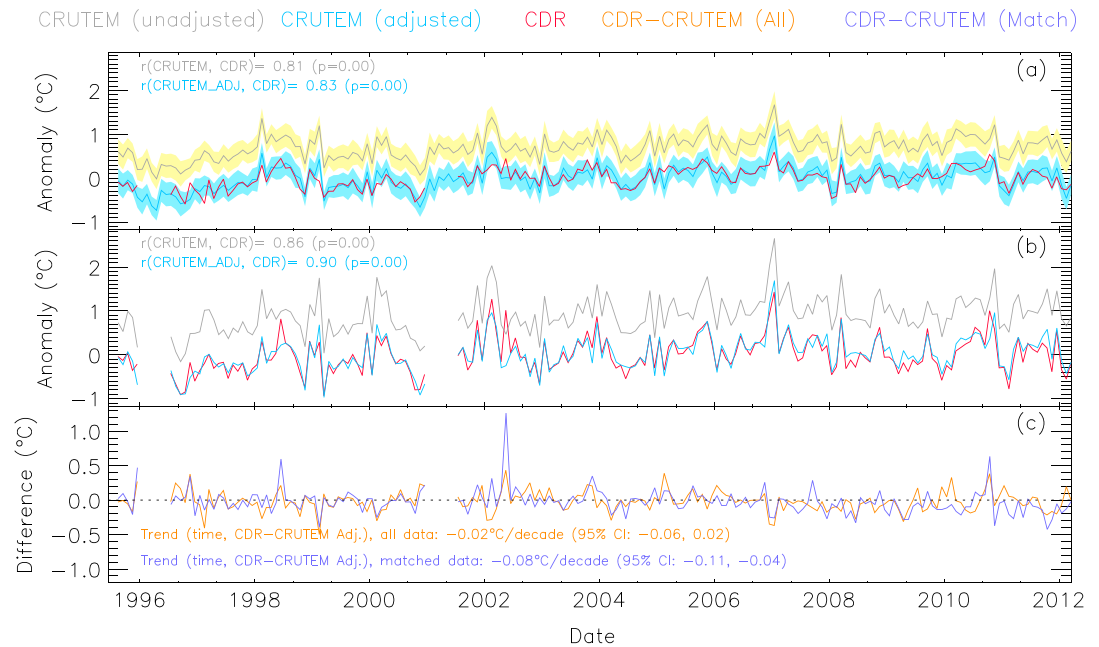**Figure 14.** As for Figure 11 but excluding LST_{day} data from the CDR time series (i.e., using only LST_{night}).

observations of T_{min} and T_{max} (section 2.3), enables a separate assessment of the stability of the CDR LST_{day} and LST_{night}. The time series at each station is compared directly with the CDR time series for the 0.05° cell nominally containing the station location. The mean LST_{night}-T_{min} trend is found to be −0.05°C/decade (n = 2122 stations), while the mean LST_{day}-T_{max} trend is −0.36°C/decade (n = 2200 stations). The more strongly negative trend for the LST_{day}-T_{max} result indicates that most of the discrepancy between the CDR and other temperature time series is due to LST_{day}. This is evidence that further supports the hypothesis that the overpass correction is introducing errors into the ATSR-2 CDR LSTs, since such errors would be more prevalent during the day, because of the dependency of LST on insolation.

Figure 14 shows the CDR and CRUTEM4 time series, but this time excluding LST_{day} from the analysis (i.e., CRUTEM4 mean monthly temperature anomalies compared with monthly CDR LST_{night} anomalies). This time series is notably more stable and less noisy than the equivalent time series in Figure 11, which is based on the mean monthly LST and therefore includes LST_{day}. The percentage of CDR anomalies that fall within the CRUTEM4 uncertainties for the adjusted time series has risen to 90%. A linear trend in the differenced time series (Figure 14c) is now undetectable using all data (−0.02°C/decade, confidence interval: −0.06 to 0.02), and a much smaller negative trend is present only in the spatially matched data (−0.08°C/decade, confidence interval: −0.11 to −0.04). The anomaly correlations with the CRUTEM4 adjusted time series have also increased to 0.83 and 0.90 for "all" and spatially matched data, respectively. Table 3, which provides the correlation coefficients and differenced time series results for different geographical regions, indicates that the improved agreement between CRUTEM4 and LST_{night} anomalies persists in all regions. Other than in the Arctic, the trends of the difference time series become less negative and/or not statistically different from zero, indicating that the agreement between the CDR and CRUTEM4 is stronger when LST_{day} is not included in the analysis.

5.2. Analysis of Grid-Cell Time Series

Figure 15 shows the relationship between the CRUTEM4 and CDR LST_{night} time series for each 5° grid cell. LST_{day} has been excluded from this analysis given the results presented in section 5.1. For most of the globe, the cell-based trends of the differenced time series (CDR minus CRUTEM4) are not statistically different from zero (indicated with an "X" in Figure 15a). Cells with both positive and negative tendencies are present, reflecting the lack of any clear linear trend in the global differenced time series shown in Figure 14. Figure 15b implies that there may be some regional variation in the median CDR minus CRUTEM4
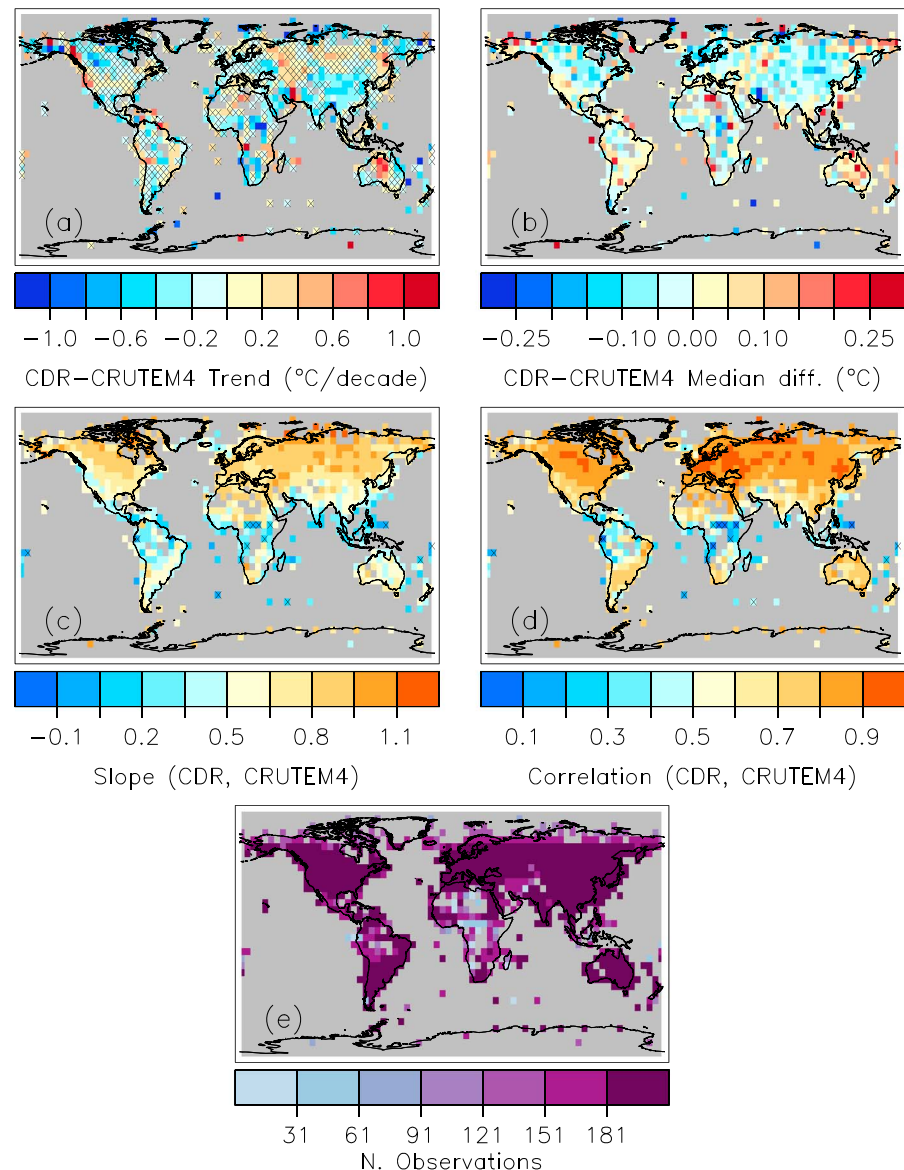
Figure 15. Maps showing the temporal relationship between (adjusted) CRUTEM4 and the CDR LST$_{night}$ anomalies (both referenced to the 1995–2012 baseline period). (a) The grid box trends of the CDR-CRUTEM4 anomaly differences, (b) the median difference in anomalies, (c) the slopes of the CDR versus CRUTEM anomalies, (d) the CDR versus CRUTEM4 anomaly correlations, and (e) the number of matched data points in each grid cell. Cells where the trends are not statistically different from zero in Figure 15a and slopes with $p > 0.05$ in Figure 15c are overlaid with an X.

anomalies. For example, the CDR anomalies tend to be warmer in Australia, while for much of Asia and North America, the CDR anomalies are cooler. However, the pattern is again generally heterogeneous.

A more consistent pattern is observed in the CRUTEM4 versus CDR slopes (Figure 15c) and correlation coefficients (Figure 15d) that reassuringly bear close resemblance to Figure 7, which shows the equivalent comparisons with CRU TS. Both correlations and slopes approach unity at mid-to-high latitudes and are significantly less than one over the tropics. The correlation coefficients are slightly lower for the CRUTEM4 comparison. This is expected, as the data presented in Figure 15 are anomalies rather than actual temperatures (CRU TS: Figure 7), so they have a smaller range and are therefore more sensitive to small variations (noise). Nevertheless, the strength of the correlations and proximity of the slopes to unity outside of the tropics suggest that both LST actual temperatures and anomalies are well aligned with T_{2m} in these regions.
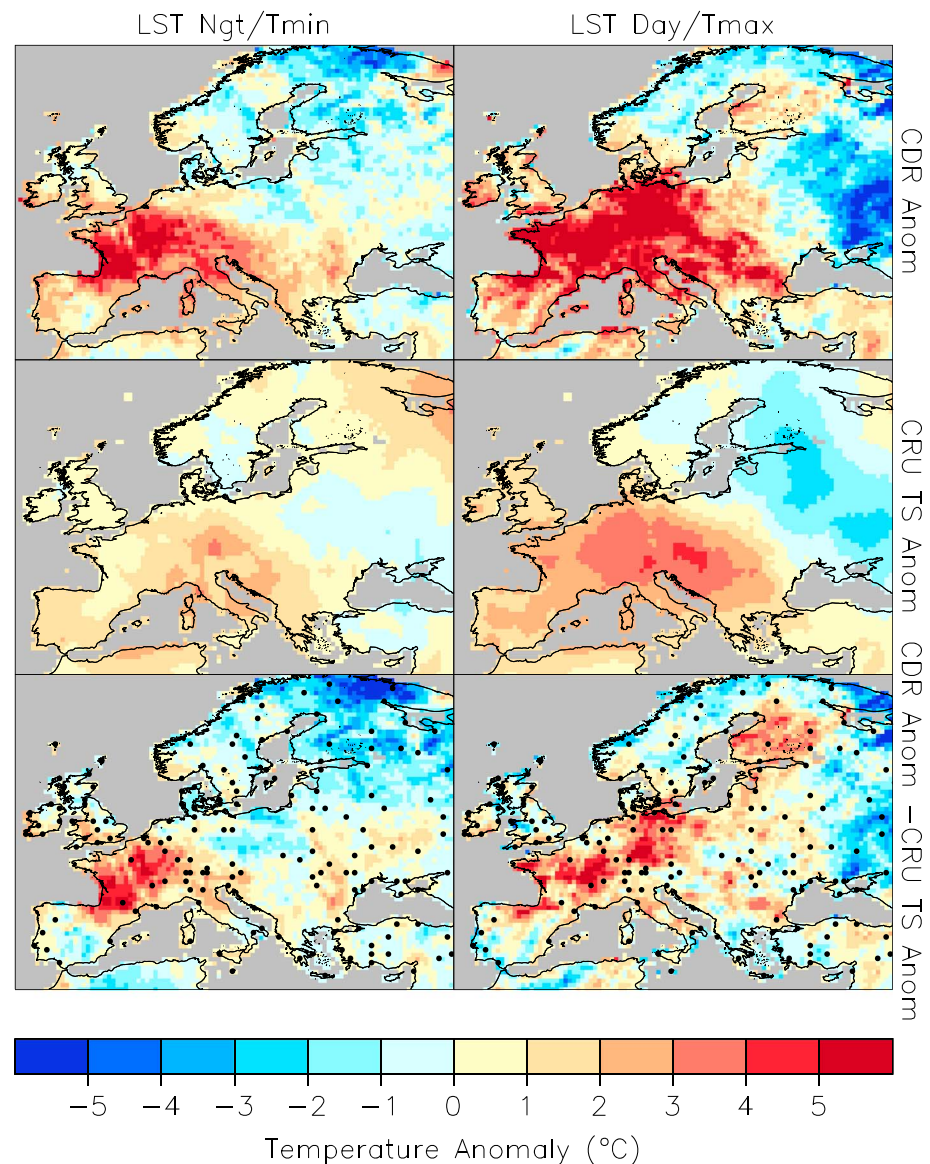
Figure 16. Temperature anomalies (°C) for the August 2003 European heave wave for (left column) LST night/T_{min} and (right column) LST day/T_{max}. Both the (top row) CDR and (middle row) CRU TS anomalies are referenced to the August 1995 to March 2012 baseline period—both are shown at a spatial resolution of 0.5°. The bottom row shows the difference between the two, with the location of the CRU TS stations overlaid (filled black circles).

6. Case Study: Europe in August 2003

Figure 16 shows the temperature anomalies from the CDR and CRU TS data sets during August 2003; the first half of this month is characterized by an extreme heat wave that affected much of Europe. The CRU TS data have been used in preference to CRUTEM4 here owing to its higher spatial resolution and availability of T_{min} and T_{max} data, which can be compared directly with the LST$_{night}$ and LST$_{day}$, respectively. It should be noted that since only monthly data are analyzed here, the results are not intended to provide full characterization of the August 2003 heat wave event.

The two data sets share many similar features. Both data sets show warm anomalies over much of Europe, which are particularly strong for LST$_{day}$/T_{max}; the presence of elevated daytime and nighttime temperatures in this month is consistent with previous studies on the August 2003 heat wave event [*Dousset et al.*, 2011; *García-Herrera et al.*, 2010]. The magnitude of the anomalies is more extreme for LST than for T_{2m}. For LST$_{day}$ this is likely to reflect the clear-sky-only data acquisition. For the LST$_{night}$/T_{min}

comparison, this is expected because LST_{night} is acquired at ~10 P.M. local solar time, when temperatures are still influenced by day time heating, whereas T_{min} typically occurs just before dawn. Therefore, as evident in Figure 16, the LST_{night} anomaly pattern shares features with both the T_{min} and T_{max} anomaly patterns.

The bottom two panels in Figure 16 show the CDR-CRU TS anomaly difference maps, with the locations of the CRU TS stations overlaid as black filled circles. CRU TS has larger uncertainties where station density is low; therefore, one might anticipate larger CDR-CRU TS differences in these areas. While the general pattern does not fully support this, most of the largest CDR-CRU TS differences do occur in station voids, for example, South-West France (LST_{night}-T_{min} only), eastern France, Central Germany (LST_{day}-T_{max} only), and northern Scandinavia/North-West Russia (Murmansk province). It is also notable from Figure 16 that the satellite data present a great deal more spatial structure and detail in the temperature variability than CRU TS.

7. Discussion: Using Satellite LSTs to Augment T_{2m} Observations

LST observed at IR wavelengths represents the temperature of the top few micrometers of the Earth's surface. From space, this corresponds to an "ensemble directional radiometric temperature," which is the aggregate of all radiometric surface temperatures within the satellite field of view in the direction of observation [*Dash et al.*, 2002; *Norman & Becker*, 1995; *Li et al.*, 2013]. Over dense vegetation, a satellite-observed LST may approximate to the canopy temperature. This is not the same as the ambient air temperature measured at weather stations at ~2 m above the Earth's surface, which has traditionally been used in climate and weather applications. In addition to this geophysical difference, satellite IR LST data are also limited to cloud-free scenes, whereas station-based T_{2m} estimates are all sky. The clear-sky bias of satellite IR data is known to affect long-term observations of upper tropospheric humidity, for example [*John et al.*, 2011], so it is natural to anticipate this may also be an issue for IR LST.

Despite these fundamental differences, the results presented here and in other studies demonstrate that satellite LST and T_{2m} are strongly related, with LST and T_{2m} closest at night, or under cloud [*Gallo et al.*, 2011; *Good*, 2015; *Good*, 2016; *Mildrexler et al.* [2011]; *Sohrabinia et al.*, 2014]. The relationship between LST_{night} and T_{min}—which are usually observed when solar heating is absent—should be less affected but not completely free from clear-sky bias because the surface cools more efficiently at night under clear skies compared with cloudy skies, leading to higher sampling of colder LSTs occurring in these conditions. The results presented in this study support this and show that the monthly CDR LST_{night} data are particularly well aligned with monthly T_{min} and even T_{mean}, in both actual temperatures and anomalies. For applications that can tolerate an uncertainty of up to 5°C, LST_{night} could provide a reasonable proxy for T_{min} for locations without ground-based observations. Where more accurate T_{min} data are required, estimates may be obtained through simple models that predict T_{min} from satellite data and other parameters, such as those proposed by *Benali et al.* [2012], *Good* [2015], etc.

The comparison between LST_{day} and T_{max} presented in this study suggests LST_{day} may also provide useful new temperature data. In areas of very dense vegetation, LST_{day} and T_{max} can be close (within a few °C). Over more sparsely vegetated and bare surfaces LST_{day} can exceed T_{max} by much more than this (up to >10°C), such that LST_{day} may not be a viable direct proxy for T_{max}. Satellite T_{2m} models can also play a role here to provide more accurate estimates of T_{max}. LST_{day} may also be biased by the clear-sky sampling, implied by the more extreme anomalies present during the August 2003 European case study introduced in section 6. However, the time series analysis of anomalies over different regions discussed in section 5.1 does not seem to show any clear-sky bias effects, which suggests that spatial averaging of anomalies may reduce the problem. However, the dependency of LST_{day} on insolation clearly causes problems in generating a temporally homogeneous LST product from sensors with different overpass times.

Given that IR satellite data offer near-complete global coverage, particularly if composited in time, there is a clear role for the use of LST data in climate and weather applications. A further benefit of satellite data over ground-based T_{2m} observations is in instrumental and methodological consistency: a single instrument with a single retrieval methodology can potentially provide a globally consistent product, whereas in situ data are

collected using different instruments at each site using different practices (e.g., observation times). A satellite data archive can also be reprocessed—for example, using an improved retrieval or calibration technique—in a consistent way, whereas in situ data often come with missing or erroneous metadata, so that applying retrospective corrections or improvements can be problematic. Lastly, satellite data are often available in very near real time, which enables a quick response time to monitoring events. For example, LST from SEVIRI is provided operationally by EUMETSAT within 2 h of acquisition. Some international station T_{2m} data, on the other hand, can take several days to weeks to be received by data producers, delaying the output of gridded data sets for monitoring. A major limitation of satellite LST data—particularly polar orbiting—is that they provide clear-sky "snapshots" in time. For the ATSR CDR, this time is at 10:00 A.M./P.M., which is a limiting factor for studies that require knowledge of maximum and minimum surface temperatures that usually occur at other times of the day. Nevertheless, this study suggests that the ATSR data can still provide useful information, particularly where the station network is sparse. It is highly unlikely that satellite LST data will ever replace conventional T_{2m} observations. However, the benefits of a synergistic approach seem clear, using multivariate station measurements as a complementary observing array that is essential to ensure adequate understanding of uncertainties in LST.

8. Conclusions and Outlook

This paper presents a comparison between a new >17 year, monthly satellite LST data set derived from the ATSR series and ground-based observations of T_{2m}. The LST-T_{2m} difference is characterized in space, by season, land cover type, vegetation fraction, and elevation. (Note that some of these influencing factors may covary, but this is not addressed here and each influence is considered separately in this study.) LST$_{night}$ is typically warmer than T_{min} (global median = 1.8°C), as expected given the ~10 P.M. local solar time satellite overpass and typical near-dawn timing of T_{min}. LST$_{night}$ is highly correlated (>0.9) and has a near one-to-one relationship with T_{min} outside of the tropics. The LST$_{night}$-T_{min} interquartile range is 3.8°C, indicating that LST$_{night}$ is often close in magnitude. This strong coupling means that for some applications, LST$_{night}$ may provide a reasonable proxy for T_{min}. The LST$_{day}$-T_{max} variability is higher (median = −0.1°C, interquartile range = 8.1°C) and more extreme: LST$_{day}$ tends to be higher than T_{max} when insolation is higher but can also be cooler, e.g., at high latitudes during winter months, or over snow or ice. LST$_{day}$ and T_{max} are not as well coupled as LST$_{night}$/T_{min}, but actual temperature correlations are still typically >0.9 at mid-to-high latitudes.

The LST-T_{2m} difference depends strongly on vegetation fraction and land cover type, particularly for LST$_{day}$/T_{max}. The largest positive LST-T_{2m} differences occur over bare surfaces: both LST$_{night}$ and LST$_{day}$ tend to be warmer than T_{min} and T_{max}, respectively, and the difference increases with decreasing solar zenith angle (higher insolation). LST-T_{2m} differences approach zero with increasing vegetation fraction. LST$_{day}$ is typically cooler than T_{max} over fully vegetated surfaces owing to surface cooling by evapotranspiration, with negative LST$_{day}$-T_{max} differences observed frequently for the forested land cover types. In contrast, LST$_{night}$ tends to be slightly warmer than T_{min} for nearly all surface types—again, this is attributed to the 10 P.M. local solar time overpass of the ATSR.

LST$_{night}$-T_{min} differences are stable with varying elevation. However, the LST-T_{2m} coupling weakens with increasing elevation, evidenced by lower correlation coefficients and regression slopes (T_{2m} versus LST). This is particularly apparent for LST$_{day}$-T_{max}.

The CDR global time series shows remarkable agreement with CRUTEM4, with a correlation between the anomaly data sets of up to 0.9 for the globe, with up to 90% of the CDR anomalies falling within the CRUTEM4 T_{2m} uncertainties. This gives useful verification of the CRUTEM4 monthly anomalies since the CDR is a completely independent data set. However, the time series analysis presented here suggests that the CDR is not free from errors arising from nonclimatic effects and there is a discrepancy between the ATSR-2 and AATSR portions of the CDR, resulting in an inhomogeneous time series. This is attributed to the overpass time correction applied by the data set providers to align the ATSR-2 data with the AATSR overpass time, which is 30 min earlier. The LST$_{night}$ time series appears more stable than the LST$_{day}$ time series, which is expected given the dependency of LST on insolation.

LST anomalies appear to be surprisingly well connected to T_{2m} anomalies in space and time. Grid-box (5° lat/lon) correlations between the CDR and CRUTEM time series are typically >0.7 and very often

>0.8 outside of the tropics. An analysis of the August 2003 European anomaly maps shows that LST anomalies quite closely resemble the equivalent T_{2m} and may add information where in situ observations are sparse. The LST maps also show more detail and structure, which will be useful where high resolution information is needed.

Although the ATSR ceased operations in 2012, the analysis presented here is relevant to the ATSR successor, SLSTR, which was launched in 2016, and other IR imagers such as MODIS and SEVIRI. It is hoped that this study will provide some of the foundation for use of LST data in climate applications. The results of this study suggest that the ATSR CDR LST_{night} may be useful for time series analysis of LST, but that LST_{day} is not temporally stable enough for this application, at least prior to the AATSR. However, the ATSR CDR LST_{day} data are still useful for other applications where temporal stability is less critical, for example, where a climatology of LST is required for knowledge of the "typical" (background) surface temperature for a particular scene, for informing gridded estimates of T_{2m}, or the study of surface fluxes through the analysis LST-T_{2m} differences. The next release of the ATSR CDR will include the uncertainties associated with the temporal correction applied to the ATSR-2 LSTs to account for the difference in ATSR-2/AATSR observation time, which should enable users to make better use of these data. It is implausible that LST will replace T_{2m} as the surface temperature variable of choice over land for many applications, since it represents a different physical quantity and has a comparatively short record length. However, it seems clear that it offers benefits both where LST is the relevant variable and in augmenting T_{2m} data from meteorological stations, particularly in data-sparse regions or where a high level of spatial detail is required.

References

Arino, O., et al. (2007), GlobCover: ESA service for global land cover from MERIS, *Geosci. Remote Sens. Symp. 2007, IEEE Int.*, doi:10.1109/IGARSS.2007.4423328.

Azevedo, J. A., L. Chapman, and C. L. Muller (2016), Quantifying the daytime and night-time urban heat island in Birmingham, UK: A comparison of satellite derived land surface temperature and high resolution air temperature observations, *Remote Sens.*, 8, 153.

Baret, F., M. Weiss, R. Lacaze, F. Camacho, H. Makhmara, P. Pacholcyzk, and B. Smets (2013), GEOV1: LAI and FAPAR essential climate variables and FCOVER global time series capitalizing over existing products. Part1: Principles of development and production, *Remote Sens. Environ.*, 137, 299–309.

Benali, A., A. C. Carvalho, J. P. Nunes, N. Carvalhais, and A. Santos (2012), Estimating air surface temperature in Portugal using MODIS LST data, *Remote Sens. Environ.*, 124, 108–121, doi:10.1016/j.rse.2012.04.024.

Bontemps, S., M. Herold, L. Kooistra, A. van Groenestijn, A. Hartley, O. Arino, I. Moreau, and P. Defourny (2012), Revisiting land cover observations to address the needs of the climate modelling community, *Biogeosci. Discuss.*, 8(4), 7713–7740, doi:10.5194/bg-9-2145-2012.

Box, J. E., and A. Rinke (2003), Evaluation of Greenland ice sheet surface climate in the HIRHAM regional climate model using automatic weather station data, *J. Clim.*, 16, 1302–1319, doi:10.1175/1520-0442-16.9.1302.

Bulgin, C. E., O. Embury, G. Corlett, and C. J. Merchant (2016), Independent uncertainty estimates for coefficient based sea surface temperature retrieval form the Along-Track Scanning Radiometer instruments, *Remote Sens. Environ.*, 178, 213–222, doi:10.1016/j.rse.2016.02.022.

Caesar, J., L. Alexander, and R. Vose (2006), Large-scale changes in observed daily maximum and minimum temperatures: Creation and analysis of a new gridded data set, *J. Geophys. Res.*, 111, D05101, doi:10.1029/2005JD006280.

Camacho, F., J. Cernicharo, R. Lacaze, F. Baret, and M. Weiss (2013), GEOV1: LAI, FAPAR essential climate variables and FCOVER global time series capitalizing over existing products. Part 2: Validation and intercomparison with reference products, *Remote Sens. Environ.*, 137, 310–329.

Casey, K. S., T. B. Brandon, P. Cornillon, and R. Evans (2010), The past, present and future of the AVHRR pathfinder SST program, in *Oceanography from Space: Revisited*, edited by V. Barale, J. F. R. Gower, and L. Alberotanza, pp. 323–341, Springer, doi:10.1007/978-90-481-8681-5_16.

Chen, F., Y. Liu, Q. Liu, and F. Qin (2014), A statistical method based on remote sensing for the estimation of air temperature in China, *Int. J. Climatol.*, doi:10.1002/joc.4113.

Dash, P., F. M. Goettsche, F. S. Olesen, and H. Fischer (2002), Land surface temperature and emissivity estimation from passive sensor data: Theory and practice-current trends, *Int. J. Remote Sens.*, 23(13), 2563–2594.

Dee, D. P., et al. (2011), The ERA-Interim reanalysis: Configuration and performance of the data assimilation system, *Q. J. R. Meteorol. Soc.*, 137, 553–597, doi:10.1002/qj.828.

De Ridder, K., C. Bertrand, G. Casanova, and W. Lefebvre (2012), Exploring a new method for the retrieval of urban thermophysical properties using thermal infrared remote sensing and deterministic modeling, *J. Geophys. Res.*, 117, D17108, doi:10.1029/2011JD017194.

Dousset, B., F. Gourmelon, K. Laaidi, K. Zeghnoun, E. Giraudet, P. Bretin, E. Mauri, and S. Vandentorren (2011), Satellite monitoring of summer heat waves in the Paris metropolitan area, *Int. J. Climatol.*, 31, 313–323, doi:10.1002/joc.2222.

Duguay-Tetzlaff, A., V. Bento, F. Göttsche, R. Stöckli, J. Martins, I. Trigo, F. Olesen, J. Bojanowski, C. da Camara, and H. Kunz (2015), Meteosat land surface temperature climate data record: Achievable accuracy and potential uncertainties, *Remote Sens.*, 7, 13,139–13,156.

Edwards, J. M., J. R. McGregor, M. R. Bush, and F. J. Bornemann (2011), Assessment of numerical weather forecasts against observations from Cardington: Seasonal diurnal cycles of screen-level and surface temperatures and surface fluxes, *Q. J. R. Meteorol. Soc.*, 137, 656–672, doi:10.1002/qj.742.

Embury, O., C. J. Merchant, and G. K. Corlett (2012), A reprocessing for climate of sea surface temperature from the along-track scanning radiometers: Initial validation, accounting for skin and diurnal variability effects, *Remote Sens. Environ.*, 116, 62–78, doi:10.1016/j.rse.2011.02.028.

Farr, T. G., and M. Kobrick (2000), Shuttle radar topography mission produces a wealth of data, *Eos Trans. AGU*, *81*(48), 583–585, doi:10.1029/EO081i048p00583.

Folwell, S., P. P. Harris, and C. M. Taylor (2016), Large-scale surface responses during European dry spells diagnosed from land surface temperature, *J. Hydrometoerol.*, *17*(3), 975–993, doi:10.1175/JHM-D-15-0064.1.

Freitas, S. C., I. F. Trigo, J. M. Bioucas-Dias, and F. M. Göttsche (2010), Quantifying the uncertainty of land surface temperature retrievals from SEVIRI/Meteosat, *IEEE Trans. Geosci. Remote Sens.*, *48*(1), 523–534.

Freitas, S. C., I. F. Trigo, J. Macedo, C. Barroso, R. Silva, and R. Perdigão (2013), Land surface temperature from multiple geostationary satellites, *Int. J. Remote Sens.*, *34*(9–10), 3051–3068, doi:10.1080/01431161.2012.716925.

García-Herrera, R., J. Díaz, R. M. Trigo, J. Luterbacher, and E. M. Fischer (2010), A review of the European summer heat wave of 2003, *Crit. Rev. Environ. Sci. Technol.*, *40*(4), 267–306, doi:10.1080/10643380802238137.

Gallo, K., R. Hale, D. Tarpley, and Y. Yu (2011), Evaluation of the relationship between air and land surface temperature under clear- and cloudy-sky conditions, *J. Appl. Meteorol. Climatol.*, *50*, 767–775.

GCOS (2016), Implementation plan 2016. [Available at http://www.wmo.int/pages/prog/gcos/.]

Ghent, D. (2012), Land surface temperature validation and algorithm verification, Report to European Space Agency. [Available at https://earth.esa.int/documents/700255/2411932/QC3_D4.1+Validation_Report_Issue_1A_20120416.pdf.]

Good, E. (2015), Daily minimum and maximum surface air temperatures from geostationary satellite data, *J. Geophys. Res. Atmos.*, *120*, 2306–2324, doi:10.1002/2014JD022438.

Good, E. (2016), An in situ-based analysis of the relationship between land surface 'skin' and screen-level air temperatures, *J. Geophys. Res. Atmos.*, *121*, 8801–8819, doi:10.1002/2016JD025318.

Good, S. A., G. K. Corlett, J. J. Remedios, E. J. Noyes, and D. T. Llewellyn-Jones (2007), The global trend in sea surface temperature from 20 years of advanced very high resolution radiometer data, *J. Clim.*, *20*, 1255–1264, doi:10.1175/JCLI4049.1.

Hachem, S., S. C. R. Duguay, and M. Allard (2012), Comparison of MODIS-derived land surface temperatures with ground surface and air temperature measurements in continuous permafrost terrain, *Cryosphere*, *6*, 51–69, doi:10.5194/tc-6-51-2012.

Hansen, J., R. Ruedy, M. Sato, and K. Lo (2010), Global surface temperature change, *Rev. Geophys.*, *48*, RG4004, doi:10.1029/2010RG000345.

Harris, I., P. D. Jones, T. J. Osborn, and D. H. Lister (2014), Updated high-resolution grids of monthly climatic observations—The CRU TS3.10 dataset, *Int. J. Climatol.*, *34*, 623–642, doi:10.1002/joc.3711.

Hartmann, D. L., et al. (2013), Observations: Atmosphere and surface, in *Climate Change 2013: The Physical Science Basis. Contribution of Working Group I to the Fifth Assessment Report of the Intergovernmental Panel on Climate Change*, edited by T. F. Stocker et al., pp. 187–189, Cambridge Univ. Press, Cambridge, U. K., and New York.

Høyer, J. L., and I. Karagali (2016), Sea surface temperature climate data record for the North Sea and Baltic Sea, *J. Clim.*, *29*, 2529–2541, doi:10.1175/JCLI-D-15-0663.1.

Hu, L., and N. Brunsell (2013), The impact of temporal aggregation of land surface temperature data for surface urban heat island (SUHI) monitoring, *Remote Sens. Environ.*, *134*, 162–174.

Hulley, G. C., S. J. Hook, E. Abbott, N. Malakar, T. Islam, and M. Abrams (2015), The ASTER Global Emissivity Dataset (ASTER GED): Mapping Earth's emissivity at 100 meter spatial scale, *Geophys. Res. Lett.*, *42*, 7966–7976, doi:10.1002/2015GL065564.

Janatian, N., M. Sadeghi, S. H. Sanaeinejad, E. Bakhshian, A. Farid, S. M. Hasheminia, and S. Ghazanfari (2016), A statistical framework for estimating air temperature using MODIS land surface temperature data, *Int. J. Climatol.*, doi:10.1002/joc.4766.

Jiménez-Muñoz, J. C., J. A. Sobrino, C. Mattar, and Y. Malhi (2013), Spatial and temporal patterns of the recent warming of the Amazon forest, *J. Geophys. Res. Atmos.*, *118*, 5204–5215, doi:10.1002/jgrd.50456.

Jin, M. (2004), Analysis of land skin temperature using AVHRR observations, *Bull. Am. Meteorol. Soc.*, *85*, 587–600, doi:10.1175/BAMS-85-4-587.

Jin, M., R. E. Dickinson, and A. M. Vogelmann (1997), A comparison of CCM2–BATS skin temperature and surface-air temperature with satellite and surface observations, *J. Clim.*, *10*, 1505–1524.

Jin, M., and R. E. Dickinson (2010), Land surface skin temperature climatology: Benefitting from the strengths of satellite observations, *Environ. Res. Lett.*, *5*, 044004, doi:10.1088/1748-9326/5/4/044004.

John, V. O., G. Holl, R. P. Allan, S. A. Buehler, D. E. Parker, and B. J. Soden (2011), Clear-sky biases in satellite infrared estimates of upper tropospheric humidity and its trends, *J. Geophys. Res.*, *116*, D14108, doi:10.1029/2010JD015355.

Jones, P. D. (1994), Hemispheric surface air temperature variations: A reanalysis and an update to 1993, *J. Clim.*, *7*, 1794–1802, doi:10.1175/1520-0442(1994)007<1794:HSATVA>2.0.CO;2.

Jones, P. D., D. H. Lister, T. J. Osborn, C. Harpham, M. Salmon, and C. P. Morice (2012), Hemispheric and large-scale land surface air temperature variations: An extensive revision and an update to 2010, *J. Geophys. Res.*, *117*, D05127, doi:10.1029/2011JD017139.

Karnieli, A., N. Agam, R. T. Pinker, M. Anderson, M. L. Imhoff, G. G. Gutman, N. Panov, and A. Goldberg (2010), Use of NDVI and land surface temperature for drought assessment: Merits and limitations, *J. Clim.*, *23*, 618–633, doi:10.1175/2009JCLI2900.1.

Kharin, V. V., F. W. Zwiers, and X. Zhang (2005), Intercomparison of near-surface temperature and precipitation extremes in AMIP-2 simulations, reanalyses, and observations, *J. Clim.*, *18*, 5201–5223, doi:10.1175/JCLI3597.1.

Kiktev, D., D. M. H. Sexton, L. Alexander, and C. K. Folland (2003), Comparison of modeled and observed trends in indices of daily climate extremes, *J. Clim.*, *16*, 3560–3571, doi:10.1175/1520-0442(2003)016<3560:COMAOT>2.0.CO;2.

Kilibarda, M., T. Hengl, G. B. M. Heuvelink, B. Gräler, E. Pebesma, M. Perčec Tadić, and B. Bajat (2014), Spatio-temporal interpolation of daily temperatures for global land areas at 1km resolution, *J. Geophys. Res. Atmos.*, *119*, 2294–2313, doi:10.1002/2013JD020803.

Koch, J., A. Siemann, S. Stisen, and J. Sheffield (2016), Spatial validation of large-scale land surface models against monthly land surface temperature patterns using innovative performance metrics, *J. Geophys. Res. Atmos.*, *121*, 5430–5452, doi:10.1002/2015JD024482.

Lawrimore, J. H., M. J. Menne, B. E. Gleason, C. N. Williams, D. B. Wuertz, R. S. Vose, and J. Rennie (2011), An overview of the Global Historical Climatology Network monthly mean temperature data set, version 3, *J. Geophys. Res.*, *116*, D19121, doi:10.1029/2011JD016187.

Li, Z.-L., B.-H. Tang, H. Wu, H. Ren, G. Yan, Z. Wan, I. F. Trigo, and J. A. Sobrino (2013), Satellite-derived land surface temperature: Current status and perspectives, *Remote Sens. Environ.*, *131*, 14–37, doi:10.1016/j.rse.2012.12.008.

Lian, X., Z. Lian, Y. Zeng, S. Yao, K. W. Peng, and S. Piao (2017), Spatiotemporal variations in the difference between satellite-observed daily maximum land surface temperature and station-based daily maximum near-surface air temperature, *J. Geophys. Res. Atmos.*, *122*, 2254–2268, doi:10.1002/2016JD025366.

Llewellyn-Jones, D., M. C. Edwards, C. T. Mutlow, A. R. Birks, I. J. Barton, and H. Tait (2001), AATSR: Global-change and surface-temperature measurements from Envisat, *ESA Bull.*, *105*, 11–21.

Merchant, C. J., et al. (2012), A 20 year independent record of sea surface temperature for climate from Along-Track Scanning Radiometers, *J. Geophys. Res.*, *117*, C12013, doi:10.1029/2012JC008400.

Merchant, C. J., et al. (2014), Sea surface temperature datasets for climate applications from Phase 1 of the European Space Agency Climate Change Initiative (SST CCI), *Geosci. Data J.*, *1*(2), 179–191, doi:10.1002/gdj3.20.

Mildrexler, D. J., M. Zhao, and S. W. Running (2011), A global comparison between station air temperatures and MODIS land surface temperatures reveals the cooling role of forests, *J. Geophys. Res.*, *116*, G03025, doi:10.1029/2010JG001486.

Mühlbauer, S., A. C. Costa, and M. Caetano (2016), A spatiotemporal analysis of droughts and the influence of North Atlantic Oscillation in the Iberian Peninsula based on MODIS imagery, *Theor. Appl. Climatol.*, *124*(3), 703–721, doi:10.1007/s00704-015-1451-9.

Norman, J. M., and F. Becker (1995), Terminology in thermal infrared remote sensing of natural surfaces, *Agric. For. Meteorol.*, *77*, 153–166.

Oku, Y., H. Ishikawa, S. Haginoya, and Y. Ma (2006), Recent trends in land surface temperature on the Tibetan Plateau, *J. Clim.*, *19*, 2995–3003, doi:10.1175/JCLI3811.1.

Oyler, J. W., A. Ballantyne, K. Jencso, M. Sweet, and S. W. Running (2015), Creating a topoclimatic daily air temperature dataset for the conterminous United States using homogenized station data and remotely sensed land skin temperature, *Int. J. Climatol.*, *35*, 2258–2279, doi:10.1002/joc.4127.

Parmentier, B., B. J. McGill, A. M. Wilson, J. Regetz, W. Jetz, R. Guralnick, M.-N. Tuanmu, and M. Schildhauer (2015), Using multi-timescale methods and satellite-derived land surface temperature for the interpolation of daily maximum air temperature in Oregon, *Int. J. Climatol.*, *35*, 3862–3878, doi:10.1002/joc.4251.

Prata, A. (2002), Land surface temperature measurement from space: AATSR algorithm theoretical basis document, Contract Report to ESA, CSIRO Atmospheric Research, Aspendale, Victoria, Australia.

Prigent, C., C. Jimenez, and F. Aires (2016), Toward "all weather," long record, and real-time land surface temperature retrievals from microwave satellite observations, *J. Geophys. Res. Atmos.*, *121*, 5699–5717, doi:10.1002/2015JD024402.

Poulter, B., et al. (2015), Plant functional type classification for earth system models: Results from the European Space Agency's land cover climate change initiative, *Geosci. Model Dev. Discuss.*, *8*(1), 429–462, doi:10.5194/gmdd-8-429-2015.

Rayner, N. A., D. E. Parker, E. B. Horton, C. K. Folland, L. V. Alexander, D. P. Rowell, E. C. Kent, and A. Kaplan (2003), Global analyses of sea surface temperature, sea ice, and night marine air temperature since the late nineteenth century, *J. Geophys. Res.*, *108*(D14), 4407, doi:10.1029/2002JD002670

Reynolds, R. W., N. A. Rayner, T. M. Smith, D. C. Stokes, and W. Wang (2002), An improved in situ and satellite SST analysis for climate, *J. Clim.*, *15*, 1609–1625, doi:10.1175/1520-0442(2002)015<1609:AIISAS>2.0.CO;2.

Rodriguez, E., C. S. Morris, J. E. Belz, E. C. Chapin, J. M. Martin, W. Daffer, S. Hensley (2005), An assessment of the SRTM topographic products, Tech. Rep. JPL D-31639, Jet Propulsion Laboratory.

Sen, P. K. (1968), Estimates of the regression coefficient based on Kendall's tau, *J. Am. Stat. Assoc.*, *63*, 1379–1389.

Singh, R., C. Singh, S. P. Ojha, A. S. Kumar, C. M. Kishtawal, and A. S. K. Kumar (2016), Land surface temperature from INSAT-3D imager data: Retrieval and assimilation in NWP model, *J. Geophys. Res. Atmos.*, *121*, 6909–6926, doi:10.1002/2016JD024752.

Smith, D., C. Mutlow, J. Delderfield, B. Watkins, and G. Mason (2012), ATSR infrared radiometric calibration and in-orbit performance, *Remote Sens. Environ.*, *116*, 4–16, doi:10.1016/j.rse.2011.01.027.

Smith, T. M., R. W. Reynolds, T. C. Peterson, and J. Lawrimore (2008), Improvements to NOAA's historical merged land–ocean surface temperature analysis (1880–2006), *J. Clim.*, *21*, 2283–2296, doi:10.1175/2007JCLI2100.1.

Sohrabinia, M., P. Zawar-Reza, and W. Rack (2014), Spatio-temporal analysis of the relationship between LST from MODIS and air temperature in New Zealand, *Theor. Appl. Climatol.*, doi:10.1007/s00704-014-1106-2.

Stull, R. (2015), *Practical Meteorology: An Algebra-Based Survey of Atmospheric Science*, 938 pp., Univ. of British Columbia, Vancouver, Canada. [Available at https://www.eoas.ubc.ca/books/Practical_Meteorology/prmet/PracticalMet_WholeBook-v1_00b.pdf.]

Sun, Z., Q. Wang, O. Batkhishig, and Z. Ouyang (2015), Relationship between evapotranspiration and land surface temperature under energy- and water-limited conditions in dry and cold climates, *Adv. Meteorol.*, *2016*, doi:10.1155/2016/1835487.

Trigo, I. F., I. T. Monteiro, F. Olesen, and E. Kabsch (2008), An assessment of remotely sensed land surface temperature, *J. Geophys. Res.*, *113*, D17108, doi:10.1029/2008JD010035.

Urban, M., J. E. C. Hüttich, C. Schmullius, and M. Herold (2013), Comparison of satellite-derived land surface temperature and air temperature from meteorological stations on the Pan-Arctic scale, *Remote Sens.*, *5*, 2348–2367, doi:10.3390/rs5052348.

Vancutsem, C., P. Ceccato, T. Dinku, and S. J. Connor (2010), Evaluation of MODIS land surface temperature data to estimate air temperature in different ecosystems over Africa, *Remote Sens. Environ.*, *114*(2), 449–465, doi:10.1016/j.rse.2009.10.002. [Available at http://www.sciencedirect.com/science/article/pii/S0034425709003113.]

Wan, Z. (2013), Collection 6 MODIS land surface temperature products Users' guide. [Available at http://www.icess.ucsb.edu/modis/LstUsrGuide/MODIS_LST_products_Users_guide_Collection-6.pdf.]

Wan, Z. (2014), New refinements and validation of the collection-6 MODIS land-surface temperature/emissivity product, *Remote Sens. Environ.*, *140*, 36–45.

Yan, Z., Z. Li, Q. Li, and P. Jones (2010), Effects of site change and urbanisation in the Beijing temperature series 1977–2006, *Int. J. Climatol.*, *30*, 1226–1234, doi:10.1002/joc.1971.

Zavody, A. M., C. T. Mutlow, and D. T. Llewellyn-Jones (1995), A radiative transfer model for sea surface temperature retrieval for the along-track scanning radiometer, *J. Geophys. Res.*, *100*(C1), 937–952, doi:10.1029/94JC02170.

Zhang, W., Z. Y. Huang, Y. Yu, and W. Sun (2011), Empirical models for estimating daily maximum, minimum and mean air temperatures with MODIS land surface temperatures, *Int. J. Remote Sens.*, *32*(24), 9415–9440, doi:10.1080/01431161.2011.560622.